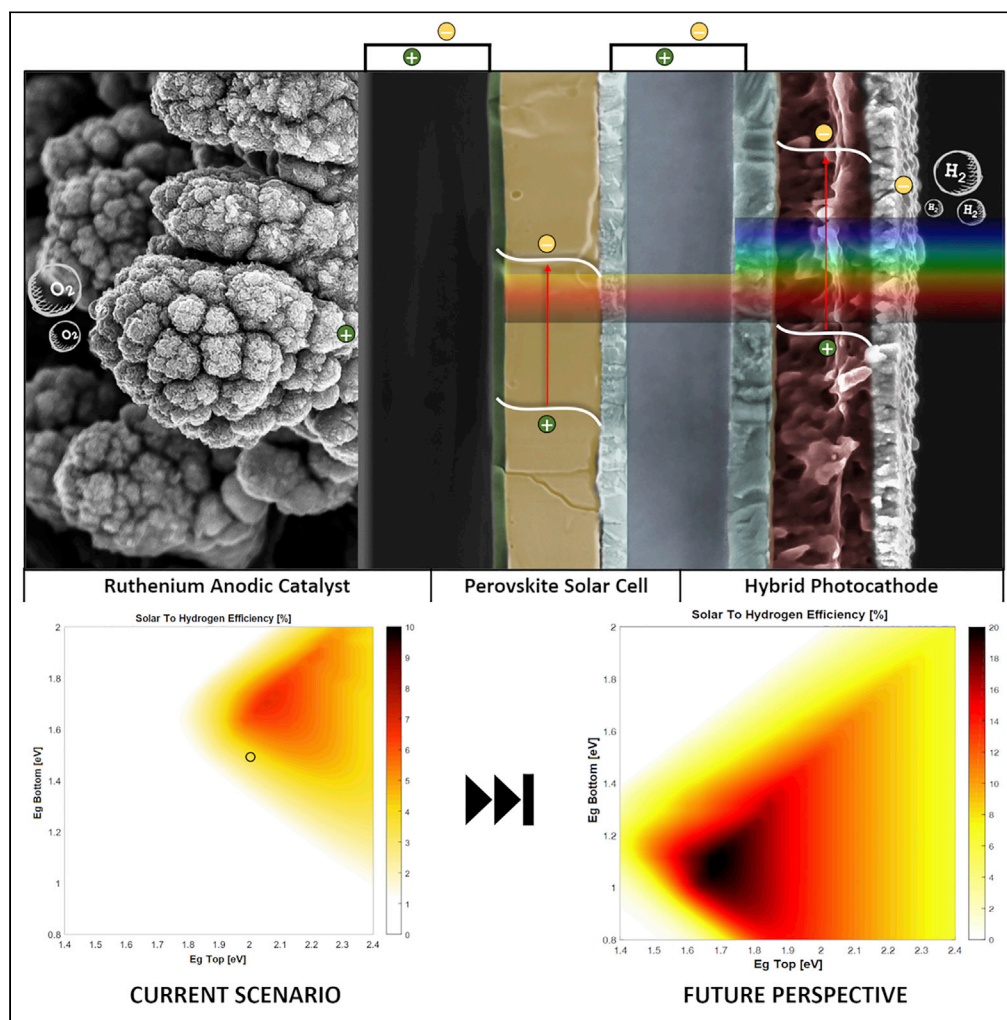


Article

Photoelectrochemical water splitting by hybrid organic-inorganic systems: setting the path from 2% to 20% solar-to-hydrogen conversion efficiency



Antonio Alfano,
Alessandro
Mezzetti,
Francesco
Fumagalli, Chen
Tao, Eugenio
Rovera,
Annamaria
Petrozza, Fabio Di
Fonzo

fabio.difonzo@iit.its

Highlights

2% STH efficiency with a hybrid photocathode/ perovskite solar cell tandem system

Multi-variable optimization tool used to find the optimal parameters to maximize STH

Optimized photocathode parameters are found in order to reach the 10% STH goal

Long-term scenario with 20% STH is predicted for hybrid organic tandem systems

Alfano et al., iScience 24,
102463
May 21, 2021 © 2021
[https://doi.org/10.1016/
j.isci.2021.102463](https://doi.org/10.1016/j.isci.2021.102463)

Article

Photoelectrochemical water splitting by hybrid organic-inorganic systems: setting the path from 2% to 20% solar-to-hydrogen conversion efficiency

Antonio Alfano,^{1,2} Alessandro Mezzetti,¹ Francesco Fumagalli,^{1,3} Chen Tao,⁴ Eugenio Rovera,¹ Annamaria Petrozza,¹ and Fabio Di Fonzo^{1,5,*}

SUMMARY

Promoting solar fuels as a viable alternative to hydrocarbons calls for technologies that couple efficiency, durability, and low cost. In this work we elucidate how hybrid organic-inorganic systems employing hybrid photocathodes (HPC) and perovskite solar cells (PSC) could eventually match these needs, enabling sustainable and clean hydrogen production. First, we demonstrate a system comprising an HPC, a PSC, and a Ru-based oxygen evolution catalyst reaching a solar-to-hydrogen (STH) efficiency above 2%. Moving from this experimental result, we elaborate a perspective for this technology by adapting the existing models to the specific case of an HPC-PSC tandem. We found two very promising scenarios: one with a 10% STH efficiency, achievable using the currently available semiconducting polymers and the widely used methylammonium lead iodide (MAPI) PSC, and the other one with a 20% STH efficiency, requiring dedicated development for water-splitting applications of recently reported high-performing organic semiconductors and narrow band-gap perovskites.

INTRODUCTION

The recent drop in the price of photovoltaics and the development of new technologies prompted photovoltaic (PV)-biased water electrolysis as a viable, near-term solution to produce green hydrogen. Several authors reported embodiments with commercial components (Clarke et al., 2009; Urbain et al., 2016), as well as with non-commercial ones. Solar-to-hydrogen (STH) efficiencies above 30% under solar concentration have been obtained (Jia et al., 2016), demonstrating the feasibility of this technology. Nevertheless, these systems are not fundamentally different from the already investigated approaches that rely on the coupling of two systems: the first that externally supplies the required voltage and the second that performs the electrolysis of water. Furthermore, the cost of the produced hydrogen is still far from the goal of 12.1 \$/kg of H₂ (Shaner et al., 2016).

An alternative approach, yet more scientifically challenging, is to develop an integrated photoelectrochemical (PEC) device, or artificial leaf. Ideally, these devices should have simple fabrication, have low cost, and be efficient, compact, with no external bias required, and intrinsically durable, possibly avoiding the stringent need for protective coatings. To pursue the goal of a PEC-water-splitting (WS) system with appreciable STH efficiency, lots of efforts have been dedicated to the design and optimization of two-photoelectrode systems, while several techno-economic analysis addressed the forecasted scenario in terms of cost, efficiency, and service-life balance to make this technology viable on a large scale (Pinaud et al., 2013; Sathre et al., 2014; Shaner et al., 2016). Throughout the years, inorganic materials—mainly oxides—have been thoroughly investigated, but results lagged behind expectations with a yield of less than 1% STH for full PEC tandem system (Bornoza et al., 2014; Chen et al., 2018a; dos Santos et al., 2018; Xu et al., 2016).

Only recently, Pan et al. (2018) successfully designed a full PEC system with all-oxide photoelectrodes, which exhibited a 3% STH efficiency. Their approach leveraged on the influence that specifically designed interlayers exert on the photocathode V_{OC} and stability. Nevertheless, many issues remain to be solved, above all the imperative necessity to protect the active layer (Cu₂O in the case of Pan's system) with barrier coatings.

¹Centre for Nano Science and Technology @PoliMi, Istituto Italiano di Tecnologia, Via Pascoli 70/3, 20133 Milano, Italy

²Politecnico di Milano, Dipartimento di Fisica, P.zza L. da Vinci 32, 20133 Milano, Italy

³European Commission Joint Research Centre (JRC), Via E. Fermi 2749, 21027 Ispra, VA, Italy

⁴School of Physics and Technology, Wuhan University, Wuhan 430072, People's Republic of China

⁵Lead contact

*Correspondence:
fabio.difonzo@iit.its

<https://doi.org/10.1016/j.isci.2021.102463>



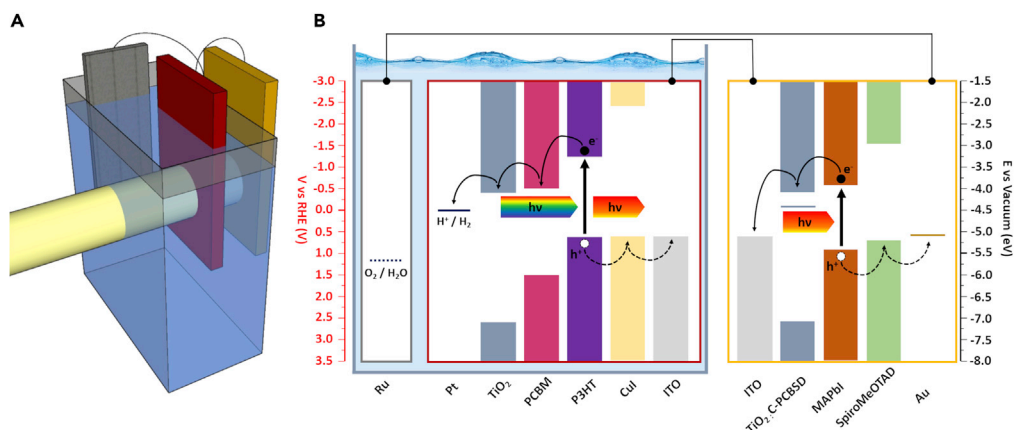


Figure 1. Representation of the tandem system

(A and B) Representation of the tandem system (A) as a 3D sketch showing the effective electrical connection and optical arrangement during measurement and (B) as a schematic that depicts the materials, energy levels and interconnections of the system elements, as well as electron (solid arrows) and hole (dashed arrows) charge flow during operation.

A compromise between the full PEC water splitting and the PV-biased water electrolysis is to realize hybrid PEC/PV systems. The PV module is here employed to provide the photovoltage required to allow water splitting to occur only by conversion of sunlight. A recent and comprehensive comparison, among these different approaches, has been provided by [Chen et al., \(2020\)](#). It is worth highlighting that, thanks to excellent performances of III-V semiconductors-based solar cells, the PEC/PV approach is currently returning promising results. Monolithic systems ([Cheng et al., 2018b](#)) and integrated PEC modules under light concentration ([Tembhurne et al., 2019](#)) reached STH efficiency as high as 19% and 17.12%. Despite these remarkable results, the inherent limit of these systems is tied to the nature of the employed photoactive layers. The high intrinsic cost of these materials, the energy demanding fabrication process, and the low defect tolerance of the whole assembly often outweigh the high STH achievable due to the increased overall system cost, which, in turn, raises the final cost of hydrogen produced ([Bellani et al., 2019](#); [Steier and Holliday, 2018](#); [Yao et al., 2018](#)). New systems are therefore required to match the target cost to make PEC hydrogen truly competitive.

In this regard, organic semiconductors-based tandem systems may represent an alternative in the field of PEC water splitting, especially in view of the recent breakthrough in high-efficiency organic photovoltaic (OPV) and perovskite solar cells (PSC). In a field dominated by devices produced with inorganic semiconductors, often processed at high temperature, this may represent a complete change of paradigm capable of bridging excellent performances with convenient fabrication techniques. To put this in perspective, recent techno-economic analysis on the forecasted price of OPV tandem moduli estimated that, for fully-upscaled devices, the final cost could be as low as 8 \$/m² ([Machui et al., 2014](#)). Same holds true for PSC, for which the estimated module cost has been set to 31.7 \$/m² to meet the market needs ([Song et al., 2017](#)). It is clear that the sum of these two values is well below the target value of 153\$/m² identified in previous studies ([Pinaud et al., 2013](#)) for large-scale PEC-WS, with sufficient margin for any additional costs it may require for this specific embodiment. Moreover, hybrid organic-inorganic PEC photocathodes, advanced in recent years from a short circuit current of 1 mA/cm² and an onset potential of 0.67 V_{RHE} ([Fumagalli et al., 2016](#)) to 8 mA/cm² at 0 V_{RHE} and an onset voltage of 0.7 V_{RHE} ([Rojas et al., 2016](#)), are approaching oxides' ([Luo et al., 2016](#)) or III-V semiconductors' ([Young et al., 2017](#)) level of performance. These results have been achieved via careful architecture engineering. Indeed, it has been demonstrated that similarly to OPV cells, hybrid photocathodes (HPC) performances can be increased by properly designing charge-selective contacts, which can efficiently extract photogenerated charge carriers from the bulk heterojunction (BHJ). As a result, the widely adopted device architecture employs a transparent conductive oxide (TCO), a hole selective layer (HSL), a BHJ, an electron selective layer (ESL), and a hydrogen evolution catalytic layer. A schematic of this structure can be seen in [Figure 1](#), where the materials used in this work are also reported alongside with a representation of the charge flow within the structure. A more detailed description of the HPC structure is provided in the HPC section. These studies also demonstrated that organic semiconductors can operate in aqueous environment without degradation, with the main stability issues coming from

the HSL or due to excessive charge accumulation at the semiconductor/electrolyte interface. In fact, more than 10 h of operational stability at pH 1 have been obtained (Mezzetti et al., 2017) on a photocathode employing a poly(3-hexylthiophene-2,5-diyl): [6,6]- phenyl C₆₁ butyric acid methyl ester (P3HT:PCBM) BHJ when coupled with an electrochemically stable WO₃ HSL. Similarly, continuous hydrogen evolution over more than 20 h with a maximum current density of 8 mA/cm² has been recently demonstrated via careful optimization of the charge extraction process at the BHJ/catalyst interface (Yao et al., 2020). However, this result has been achieved at the expenses of the optical transparency of the device, thus preventing it to be employed in tandem configuration with other photoactive components. Furthermore, the potential for all-solution, large-area processing (Bellani et al., 2017; Rojas et al., 2017) and improved light harvesting with nanostructured scaffolds (Ghadirzadeh et al., 2018; Steier et al., 2017) has been demonstrated as well. A comprehensive review of state of the art of organic semiconductor-based water splitting can be found in several literature reviews recently published (Bellani et al., 2019; Otep et al., 2020; Steier and Holliday, 2018; Yao et al., 2018).

The continuous development of materials and architectures experienced in the field of OPV— recently achieving efficiencies as high as 17.3% (Meng et al., 2018) and 15.7% (Yuan et al., 2019) for tandem and single junction moduli—bodes well for the akin field of Hybrid Organic Photoelectrochemical (HOPEC) devices. Unfortunately, organic-based photoanodes lag behind in development, with very few, low-performance systems demonstrated so far (Bornož et al., 2015; Gu et al., 2017; Kirner et al., 2014; Wang et al., 2018). At the state of the art, a solar-powered full water-splitting device based solely on HOPEC has never been demonstrated.

On the other hand, PSCs are pushing the limits of hybrid organic inorganic systems for solar energy conversion to new standards, rivalling inorganic-based systems. Consequently, PSCs are being adopted also in PEC/PV systems rather than only for PV biased electrolysis. Interestingly, due to their high photovoltage, PSCs often allow to minimize the number of photoactive elements employed, enabling water splitting when coupled with one photoelectrode, such as Fe₂O₃- and BiVO₄-based ones (Dias et al., 2015; Gurudayal et al., 2015, 2017; Karuturi et al., 2018; Kim et al., 2015; Qiu et al., 2016).

These tandem systems are intrinsically limited by the low achievable photocurrent that the PEC component could provide and the partial overlap of the absorption spectra of the photoactive components. Specifically tailored photoelectrodes have been designed for this purpose, returning STH values of 4.6% (Li et al., 2019) when arranged in optical series with the PSC. To avoid the shortcomings of curtailed light harvesting, configurations other than the one previously discussed have been investigated. In particular, to ease the constraint of the optical transparency of the immersed photoelectrode and retain the high V_{OC} and FF of the PSC, Qiu et al. (2016) employed a beam splitter to redirect the portion of the solar spectrum with wavelength (λ) > 515 nm to the CH₃NH₃PbI₃ (MAPI) PSC and λ < 515 nm to the Mo:BiVO₄ nanostructured photoanode. This arrangement allowed reaching an STH as high as 6.2%. Semi-transparent PSCs recently allowed pushing further the value of efficiency for PV/PEC systems employing organic photoabsorbers. Indeed, by stacking two PSCs and a Sb₂Se₃ photocathode an unprecedented 10.2% STH was demonstrated (Yang et al., 2020) further closing the gap with fully inorganic PEC/PV systems (Ahmed and Dincer, 2019; Andrei et al., 2018; Chen et al., 2018b; Dias et al., 2015; Pihosh et al., 2015).

Furthermore, exploiting the absorption tunability of the organic photoactive materials and their scalable and low-cost fabrication processes can be the key to deploy this technology on large scale.

Thus, a hybrid organic-inorganic, solution-processable artificial leaf pairing a PSC and a hybrid photocathode (HPC-PSC) holds the potential of meeting these requirements.

Nevertheless, we should not forget the other two key figures of Pinaud's work, i.e., a 10% STH efficiency and a 10-year lifetime. Although a few systems nowadays overcome the first, the second is still unmet (Ahmed and Dincer, 2019).

The aim of this work is to explore the theoretical and practical efficiency limits of the envisaged HPC-PSC tandem system for full, unassisted water splitting and demonstrate the feasibility of an actual working device. The experimental results obtained for the tandem HPC-PSC cell are extrapolated by means of the model proposed by Fountaine et al. (2016), modified to explicitly take into account the organic

semiconductor physics. The obtained model is then used to study the perspective of a high-efficiency scenario in which the HPC matches the performance of the current state-of-the-art organic solar cell, ultimately achieving STH close to 20%. As a midpoint toward this ambitious goal, we identify also a 10% STH goal, which can be met in the short term and highlight the most relevant parameters that must be optimized to achieve this target.

RESULTS

HPC-PSC tandem

The three-element tandem cell has been assembled according to the 3D sketch depicted in [Figure 1A](#), alongside the detailed description of the materials employed for each layer, their energetic alignment, and the charge flow across the tandem reported in [Figure 1B](#). The Ru catalyst and the HPC are immersed in the electrolytic solution inside the quartz cell, whereas the PSC ([Tao et al., 2017](#)) is placed outside the cell; the optical path goes through the HPC (within the quartz cell) first and then through the PSC, whereas the Ru catalyst is placed sideways and out of the optical path. This configuration has been adopted for the experimental assessment of unbiased water-splitting efficiency and subsequently embedded in the theoretical description. The hybrid organic photocathode and Ru anodic electrocatalyst have been developed *ad hoc* in view of tandem system integration, whereas the MAPI PSC was fabricated according to the recipe by [Tao et al. \(2017\)](#), without any further optimization. The complete assembly is then characterized, highlighting the most relevant parameters that need to be addressed to maximize the performances of future systems. Improvement-oriented guidelines will be retrieved on the basis of a specifically tailored model, eventually used to frame a short-term new efficiency scenario as well as a future perspective for this promising system.

Hybrid organic photocathode

To be efficiently integrated within a tandem cell, several additional criteria need to be met by the photoelectrodes with respect to a stand-alone configuration. Optical transparency is the first key requirement to fulfill, especially when the photoelectrode is the first element of the optical series. Additionally, a steep photocurrent profile, namely, a rapid increase from onset values to saturation ones, is required to better exploit the voltage bias provided by the PV component and thus improve the operational work point of the overall tandem system.

In this work we set as a reference the benchmark device developed by [Rojas et al. \(2016\)](#), a hybrid photocathode that achieves exceptional results in terms of photocurrent and onset potential. Despite the excellent performance, to effectively integrate this device within the tandem cell system a step-by-step, dedicated optimization is required. The device architecture (shown in [Figure 1B](#)) comprises a In:SnO₂ TCO, a CuI HSL, a P3HT:PCBM BHJ, a TiO₂ ESL, and a Pt catalytic layer; the materials employed and their energetic alignment represent an excellent starting point for an efficient photocathode and therefore are not changed.

As already mentioned, the most stringent aspect for an effective tandem cell integration is the minimization of detrimental absorption/reflection losses. The original photocathode by Rojas employs a 10-nm-thick Pt catalytic layer, because its use as a stand-alone device posed no optical constraints. However, when employed in a tandem configuration, such a thick metallic layer would reflect a substantial part of the incoming radiation, dramatically reducing the transmitted photon flux toward the next element in the optical series, that is, the PSC. To this end, the thickness of the platinum catalytic layer was reduced from 10 nm to 4 nm, adjusting the magnetron sputtering deposition time accordingly and keeping the other deposition parameters unchanged. As shown in [Figure S1A](#), the optimized device shows a significant improvement in total transmittance compared with the original one; despite the reduced catalyst loading, the performance of the optimized device presents a slight improvement ([Figure S1B](#)). This counter-intuitive result is achieved thanks to the concomitant optimization of the underlying TiO₂ scaffold layer.

The optimization of the TiO₂ scaffold layer was aimed at enhancing the available surface area, thus exploiting more efficiently the reduced platinum loading. To this end, the TiO₂ deposition parameters have been modified from their original values ([Table S1](#)): the background gas pressure was increased and the laser fluence was reduced to lower the kinetic energy of the ablated specimen within the plasma plume and thus increase the porosity of the deposited film. The thickness of layer was left unchanged, equal to approximately 100 nm. The resulting optimized TiO₂ scaffold layer is a mesoporous film comprised by

self-assembled tree-like nanostructures (Figure S2) with a high density of nano-clusters in its topmost region that act as host binding sites for Pt atoms. As an added bonus, lowering the impact energy of the ablated specimen reduces the kinetic damage caused to the underlying layer, the polymeric bulk heterojunction in our case.

Concerning the bulk heterojunction, the optimization process involved its formulation; several works on OPV solar cells using a P3HT:PCBM BHJ suggested that a higher amount of donor material is responsible for an overall increase in the device performance. Therefore, the recipe was adjusted from the original 1:1 D/A ratio to the optimum 1:0.7 D/A ratio. Furthermore, the spin-coating protocol was modified by removing a low-speed initial step (original recipe: 800 rpm for 3 s, followed by 1,600 rpm for 60 s) and thus achieving a thinner BHJ of approximately 180 ± 10 nm. Despite the thinner BHJ, the improved charge generation and extraction provided by the new formulation grants a slight boost in performance to the device (Figure S3A).

Finally, the CuI HSL deposition protocol and TCO substrate has been modified. The original architecture employed fluorine-doped tin oxide (FTO) as the TCO over the glass substrate. However, using indium-doped tin oxide (ITO) provided a more conformal coverage of the TCO surface with the deposited CuI layer. This may be attributed to the lower R_{ms} of the ITO compared with FTO. Furthermore, a lower defectiveness of the CuI layer was obtained by performing the CuI spin coating process inside a N_2 -filled glovebox rather than in air. The occurrence of islands-like defects due to the interaction of the spin-coated CuI solution with the environmental humidity was suppressed, thus avoiding the formation of detrimental agglomerates that induced additional charge transfer resistance and improving the overall performance of the device (Figure S3B).

All the previous optimization steps are combined into the optimized photocathode used in this work; comparing the electrical performance, the polarization curves (Figure S4A) show a steeper current profile for the optimized device. This improvement can be quantified using the ratiometric power saved ϕ_{Saved} figure of merit (Coridan et al., 2015), defined as:

$$\phi_{\text{Saved}} = \frac{f_{\text{FE}} J_{\text{MPP}} V_{\text{MPP}}}{P_{\text{in}}}$$

where f_{FE} is the faradaic efficiency (which in the previous work [Rojas et al., 2016] was estimated to be $\approx 100\%$), P_{in} is the incident solar radiation, and J_{MPP} and V_{MPP} are the current density and the potential at the maximum power point (MPP), respectively.

Between the benchmark and the optimized photocathode, the MPP moves from $J_{\text{MPP}} = 3.98$ mA/cm² at $V_{\text{MPP}} = 0.303$ V_{RHE} to $J_{\text{MPP}} = 4.6$ mA/cm² at $V_{\text{MPP}} = 0.33$ V_{RHE}. The corresponding ratiometric power saved ϕ_{Saved} (Figure S4B) increases from 1.21% to 1.51%, confirming the positive results of this step-by-step, dedicated optimization.

Ruthenium OER catalyst

A ruthenium nanostructured film is employed as the anodic electrocatalyst for the oxygen evolution reaction (OER). Together with iridium, ruthenium currently represents the state-of-the-art material for OER catalysts that operate in acidic chemical environments, capable of reaching very low catalytic overpotentials when properly designed and fabricated (McCrory et al., 2015). As each component directly affects the final performance of the tandem system, the ruthenium film has been carefully optimized to reach a catalytic activity on par with the best ones reported in the literature.

The catalyst is fabricated via electrodeposition of ruthenium from aqueous solution at high cathodic overpotential, adapting the recipe by Oppedisano et al. (2014) for our application. The catalyst has been deposited on an active area of 0.066 cm² defined using a vinyl tape mask, so that it matches one of the two other components of the stack, i.e., the HPC and PSC. The best-performing device is obtained using a 0.25 M HClO₄ solution with 15 mM RuCl₃·xH₂O precursor as the electrolyte and performing the electrodeposition process with an applied bias of -5 V_{RHE} for 300 s, with a thin titanium sheet as the substrate. Under such a high cathodic bias, a vigorous production of H₂ takes place on the substrate surface, whereas the concomitant electrodeposition of ruthenium only achieves a small percent of faradaic efficiency. The heavy bubbling effectively acts as a dynamic template for the deposition of metallic ruthenium (as confirmed

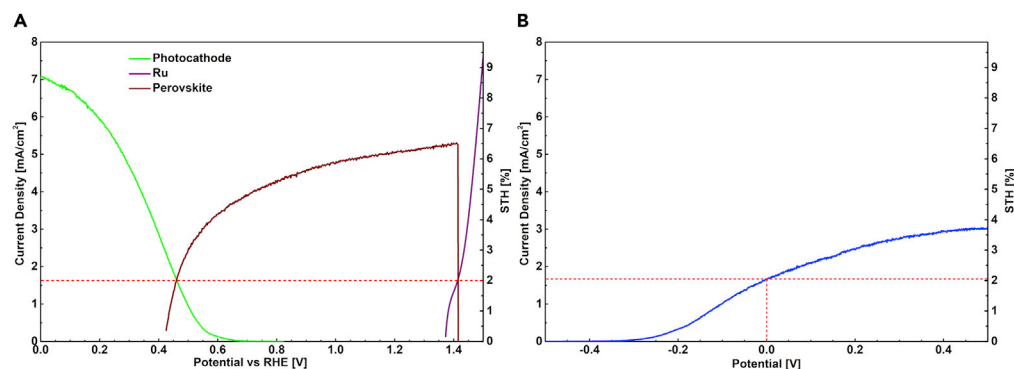


Figure 2. Current-voltage profiles

(A and B) Current-voltage profiles (A) of the three tandem system components under current matching, showing the expected working point and STH efficiency (red dotted line) and (B) of the tandem stack under operation, showing the effective operating current density and STH efficiency (red dotted line) under no applied bias.

by the X-ray diffraction spectrum of the sample in [Figure S5](#)), ultimately producing a nanostructured film with tree-like dendritic branches ([Figure S6](#)) and an estimated roughness factor of 340 ([Oppedisano et al., 2014](#)). This nanostructured ruthenium catalyst shows an overpotential η_{10} of 255 mV and a Tafel slope of $48.3 \text{ mV} \cdot \text{dec}^{-1}$ ([Figure S7A](#)), among the best values reported in the literature for ruthenium-based OER catalysts ([McCrory et al., 2015](#)). The high catalytic activity of the ruthenium electrocatalyst improves the overall performance of the tandem system by reducing the overpotential required to perform oxygen evolution at the anodic contact to the lowest value currently attainable. Despite the higher efficiency compared with ruthenium oxide, metallic ruthenium is reported to suffer long-term chemical degradation due to metal dissolution in the electrolytic environment ([Cherevko et al., 2016](#)). Nevertheless, the operative stability of such metallic catalysts is nearly 100% in the time frame explored, as reported by the chronopotentiometry measurements at $10 \text{ mA} \cdot \text{cm}^{-2}$ of our ruthenium catalyst ([Figure S7B](#)). Within the first 10 min of OER operation, the overpotential to evolve oxygen shifts by only 5 mV from its starting value of 255 mV, ensuring that the tandem system operates in a steady state for what concerns the anodic reaction, resting the dynamics of the system on the behavior of the two other components.

Artificial leaf based on the HPC-PSC tandem

The STH efficiency of the tandem cell will depend linearly on the current value obtained at the matching point between the J-V characteristics of the three components, as imposed by the electrical connection in series. The hybrid photocathode and ruthenium electrocatalyst polarization curves ([Figure 2A](#)) show an onset potential of $0.72 V_{\text{RHE}}$ and $1.38 V_{\text{RHE}}$, for the hydrogen and oxygen evolution reactions, respectively. This electrochemical configuration thus requires a minimum bias of 0.66 V to overcome the catalytic activation barrier and perform the full water-splitting reaction. The PSC provides the required minimum bias, enabling the water-splitting reaction at the two electrodes. Despite the severe performance loss introduced by the photocathode optical shadowing ([Figure S8](#)), the PSC still delivers almost 1 V of photovoltage bias and the matching point between the three J-V characteristics gives a foreseen current density of 1.6 mA/cm^2 , which corresponds to a 1.97% STH efficiency (red dotted line in [Figure 2A](#)). This efficiency value has been estimated using a conservative approach. Indeed, the polarization curves employed for the estimation are representative of the average behavior of the components they refer to, thus trying to minimize the effects of over and under estimation.

Hence, the calculated matching point of the three components describes an operating condition where no additional bias is externally provided, the so-called unbiased performance of the HPC-PSC tandem system. To validate this theoretical forecast, the assembled tandem system is characterized using linear sweep voltammetry measurements ([Figure 2B](#)). The polarization curve of the tandem system follows the evolution of its working point as the external potential overlaps (positive bias) or separates (negative bias) the J-V characteristics of the three components. With no external voltage applied, the system can perform the water-splitting reaction with an overall current of 1.65 mA/cm^2 . As a quantitative faradaic efficiency (FE) has been already measured for the photocathode alone ([Rojas et al., 2016](#)), we assume $\text{FE} = 100\%$ and hence we obtain $\text{STH} = 2.03\%$ (red lines crossing point in [Figure 2B](#)). To the best of our knowledge, this is the very

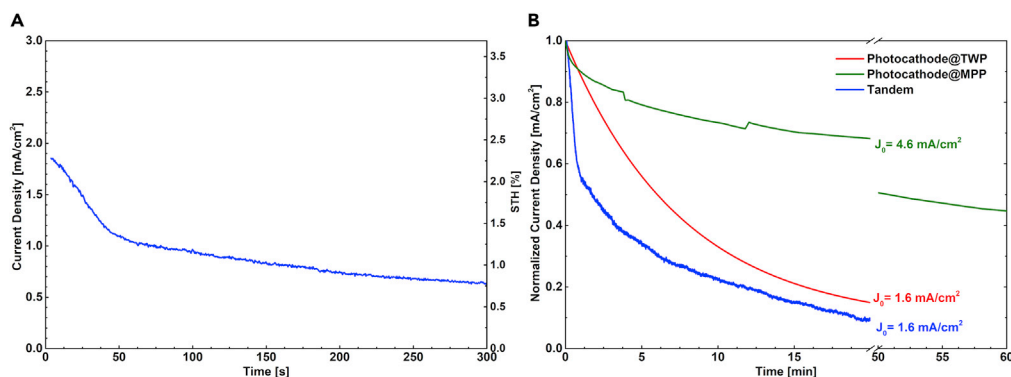


Figure 3. Chronoamperometry measurements

(A and B) Chronoamperometry measurements (A) for the PSC/HPC/Ru tandem structure under no applied bias and (B) in comparison between the normalized photocurrent time decay of the photocathode (red and green lines) and of the tandem cell (blue line). The photocurrents recorded at $t = 0$ s are reported alongside to each curve.

first demonstration of a working tandem system employing a hybrid organic photocathode and an organic-based PV cell with substantial conversion efficiency.

The temporal evolution of the system photocurrent is probed with unbiased chronoamperometric measurements (blue line in Figures 3A and 3B). The initial abrupt decrease in photocurrent is attributed to the formation of bubbles on the catalyst's surface that reduces the interface with the electrolyte and to a shift in the working point of the tandem stack. To clearly evaluate this effect, it is convenient to focus our attention on the behavior of the hybrid photocathode alone, because the other two components have been proved to suffer negligible degradation in the temporal window of interest. Chronoamperometry for the hybrid photocathode at its MPP ($= 0.33 V_{\text{RHE}}$) and at the tandem working point ($\text{TWP} = 0.45 V_{\text{RHE}}$) are reported against the one for the tandem stack (Figure 3B). The temporal evolution of the photocathode current under the two different polarization bias is remarkably different: the photocurrent after 10 min of operation is 73% and 33% of the initial value for the MPP and TWP measurements, respectively. The behavior of the photocathode polarized at the TWP and of the tandem stack is quite similar, so we can assume that both are correlated to the same phenomenon. As the TWP lies close to the V_{OC} , the effect of trap-induced losses in the BHJ amorphous mixed phase and fill factor reduction caused by an increase in bimolecular recombination due to charge accumulation is more pronounced, as reported for several OPV cells (Heumüller et al., 2014; Kawano and Adachi, 2009; Salvador et al., 2017; Wu et al., 2014). On the other hand, the photocurrent at the MPP shows a slow-decaying profile due to the intrinsic electrochemical instability of the CuI hole-extracting layer. These considerations offer an intriguing perspective on the stability improvement that could be achieved with just a 120 mV photovoltage increase, shifting the current TWP toward the hybrid photocathode MPP. Moreover, if the tandem stack could operate at the photocathode MPP, the resulting STH efficiency would be 5.67% ($J_{\text{MPP}} = 4.6 \text{ mA/cm}^2$), a 3-fold efficiency increase that is surely within reach of this technology and that is therefore accounted as a short-term perspective for the optimization of the system.

Perspective for tandem optimization

Tandem modeling

The theoretical STH efficiency that can be achieved with a PEC photoanode-photocathode and with a PV-biased system has been thoroughly described in several works (Fountain et al., 2016; Haussener et al., 2012; Holmes-Gentle and Hellgardt, 2018; Hu et al., 2013); nevertheless, these models need to be modified and adapted to take into account the specific physicochemical processes occurring in organic semiconductors. The tandem system presented in this work (Figure 1) is a two-terminal optically-in-series device where the incident light is first absorbed by the hybrid photocathode and then by the PSC, with the anodic electrocatalyst placed aside from the light path. The expected optical response of the tandem system is the superposition of the absorption profiles of its two photoactive components (Figure S9). Owing to this arrangement in series, the optical shadowing of the hybrid photocathode reduces the amount of photons reaching the PSC, lowering its electrical performance in terms of photocurrent and photovoltage. This effect is efficiently accounted for by the theoretical model of Fountain et al. (2016), which we use as the starting point to describe our HPC-PSC system, by including explicitly the physical characteristics of the organic

bulk heterojunction. The contribution in terms of photocurrent and photovoltage of the top-absorber (HPC) and the bottom absorber (PSC) is correlated to the optical band gap and absorption spectrum via the detailed balance analysis of the Shockley-Queisser (S-Q) limit:

$$J_L = q \int_{E_g}^{\infty} IPCE n_{ph}(E) dE$$

The maximum achievable photocurrent J_L is equal to the number of incident photons n_{ph} (for this application, using the AM1.5 solar irradiance spectrum) times the incident photon to current efficiency (IPCE) of a given semiconductor, integrated over all the photon energies above its optical band gap E_g .

Following the approach described by Fountaine, it is convenient to express the contribution of each photoactive component in terms of voltage. In this way, it is possible to describe the current-voltage characteristic through the inverse formulation of the diode equation:

$$V_{PV}(j) = \frac{n_d k_B T}{q} \ln \left[\frac{f_{abs} J_L - j - \frac{(V_{PV} + j R_s)}{R_{sh}}}{J_0 / ERE} + 1 \right] - j R_s$$

where n_d is the diode ideality factor, k_B is the Boltzmann constant, T the device temperature, f_{abs} is the semiconductor absorption fraction, ERE is the external radiative efficiency, J_0 is the dark current, and R_s and R_{sh} are the series and shunt resistances, respectively. To describe the anodic $V_{cat,a(j)}$ and cathodic $V_{cat,c(j)}$ catalytic overpotentials, we adopt the approximated formulation of the inverse Butler-Volmer equation^[46]:

$$V_{cat}(j) = \frac{RT}{\alpha n_e F} \sinh^{-1} \left(\frac{j}{2J_{0,cat}} \right)$$

where α is the charge transfer coefficient, n_e is the number of electrons taking part in the reaction, F is the Faraday constant, and $J_{0,cat}$ is the catalytic exchange current density.

The photovoltage of the hybrid photocathode can be described as the superposition of the diode equation and the Butler-Volmer equation for the cathodic catalytic reaction:

$$V_{HPC}(j) = V_{PV} - V_{cat,c}$$

It is now necessary to depart from the aforementioned approach and to take into account the peculiar behavior of organic semiconductors: the maximum photovoltage from a given BHJ is strictly correlated to the energy difference between the highest occupied molecular orbital (HOMO) of the donor and the lowest unoccupied molecular orbital (LUMO) of the acceptor, minus the voltage loss (V_{LOSS}) arising from the non-ideality of the system.

$$V_{OC} = \frac{1}{e} (E_{A,LUMO} - E_{D,HOMO}) - V_{LOSS}$$

The voltage loss accounts for the energy lost both during charge generation and charge recombination. Understating the insurgence of these phenomena is one of the hot topics in the field of OPV, as it represents a significant barrier toward the implementation of high power conversion efficiency (PCE) moduli. Including this parameter in the model is therefore essential to effectively describe the maximum photovoltage values that can be achieved by the system.

The overall voltage provided by the HPC-PSC tandem system must overcome the required electrochemical potential of $E_{WS} = 1.23 V_{RHE}$ for the water-splitting reaction to occur:

$$V_{HPC-PSC}(j) = V_{PV}(j) + V_{HPC}(j) - V_{cat,a}(j) \geq E_{WS}$$

The maximum efficiency is achieved when the photovoltage is equal to the water-splitting potential and the operating current density at this potential is directly proportional to the STH efficiency of the system, through the formula:

$$\eta_{STH} = \frac{J_{op} E_{WS} f_{FE}}{P_{in}}$$

Table 1. Parameters employed to simulate the current state of the HPC-PSC tandem cell

	HPC	PSC
Normalized R_s	0.15	0.05
Normalized R_{sh}	10^2	10^2
$V_{Loss}[V]$	0.41	–
IPCE	0.55	0.8
ERE	10^{-7}	10^{-5}
$J_{cat,c}[mA/cm^2]$	0.25	–
$J_{cat,a}[mA/cm^2]$	0.01	–

IPCE values in the table are taken from (Rojas et al., 2016; Tao et al., 2017).

where J_{op} is the operating current density, E_{WS} is the water-splitting potential of 1.23 V_{RHE} , f_{FE} is the Faradaic efficiency, and P_{in} is the incident solar power.

Several scenarios can be depicted, based on the ideality degree of the parameters describing the components within the system. For the anodic electrocatalyst, the reaction overpotential is intrinsically connected to the material employed. Concerning the PSC and the photocathode, the parameters of the model are the IPCE, ERE, n_d , j_0 , V_{LOSS} , and normalized R_s and R_{sh} . Additionally, as the hybrid photocathode also performs the hydrogen evolution reaction, the parameters describing the reaction overpotentials, namely, $J_{0,cat,c}$ and α , are also included in the model. The ideal case (Figure S10), corresponding to the one showed in the work of Fountaine et al. (2016) was used as the benchmark model to validate our description. To tailor the model to our specific system, each component (i.e., the hybrid photocathode, the PSC, and the ruthenium electrocatalyst) is thoroughly characterized and the parameters are extracted from the experimental data.

Tandem simulation: current state

For both the hybrid organic photocathodes, the PSC and the Ru electrocatalyst, the parameters for the simulation (Table 1) have been obtained from fitting the polarization curves shown in Figure 2A according to the aforementioned model, complemented, where needed, with values taken from the already published works concerning those architectures. We then modeled the current-voltage behavior of the system, retrieving the STH efficiency as a function of the band gap of two absorbers (Figure 4). For our case, the top absorber is the P3HT:PCBM bulk heterojunction of the hybrid photocathode ($E_g \approx 2$ eV) and the bottom absorber is the MAPI of the PSC ($E_g \approx 1.5$ eV), resulting in a forecasted STH efficiency around 2%, as highlighted by the black dot in the contour plot. This value is in excellent agreement with the experimental result, from which we can infer the validity of the model in describing the behavior of our system. An additional information that can be retrieved from this plot is that a 5.85% STH efficiency can be achieved with the current set of optoelectronic parameters, provided the top absorber has a 2.16 eV band gap and the bottom absorber has a 1.8 eV band gap. These higher band gap values are needed to provide additional photovoltage and thus to further overcome existing voltage losses.

Short-term tandem optimization

As the minimum conversion efficiency required to be competitive with a PV plus electrolyser system for green H_2 generation has been estimated as 10% STH (Pinaud et al., 2013), we use our model to identify the most critical parameters that are currently limiting the performances. This in turn allows us to define an effective optimization pathway, focused on solving first these critical issues as a gateway toward a fast STH increase. As discussed in the previous sections, our model precisely describes the current situation. Indeed, theoretical versus experimental STH are in excellent agreement. Thus, evaluating the STH partial derivatives (Table S2) with respect to the optoelectronic parameters employed to shape the current-state scenario is an effective way to perform a sensitivity analysis. This efficiently returns meaningful information on where attention should be focused. For each HPC-related variable P_i (such as R_s , R_{sh} , IPCE, V_{LOSS} , $J_{cat,c}$) affecting the STH efficiency, the Newton's difference quotient method with a 0.5% differential is employed. The magnitude of $|\partial STH/\partial P_i|$ is thus directly correlated to the weight that P_i exerts on STH. The higher its value, the stronger the influence that a slight P_i variation will have on the STH increase. Of the optoelectronic parameters analyzed, the normalized series resistance R_s , the voltage loss V_{LOSS} , and the internal conversion efficiency IPCE are found to exercise the strongest influence on the STH efficiency of

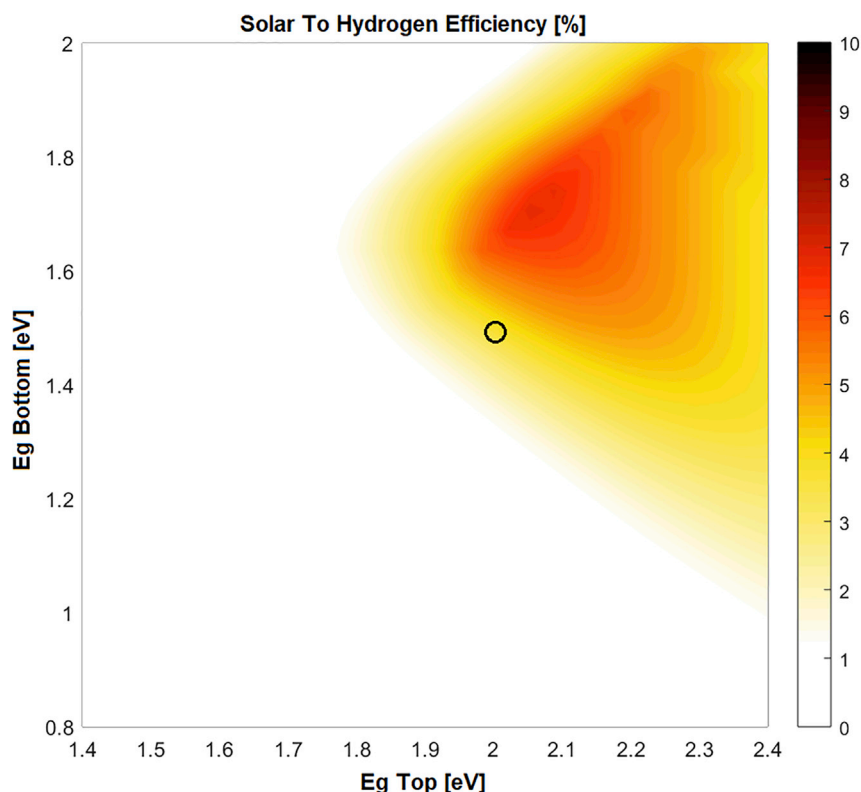


Figure 4. STH efficiency as a function of the band gap of top and bottom absorbers considering the extrapolated parameters

The black circle identifies the condition of the HPC and PSC employed in this work.

the system. Hence, the parameters are improved accordingly, until reaching a new set of values (reported in Table 2) where our HPC-PSC tandem reaches the 10% STH target. While doing this optimization R_s , V_{Loss} , and IPCE improvements were privileged over the other parameters as highlighted by the sensitivity analysis. In turn, this set of parameters is used for a further band-gap optimization (Figure 5). In this optimized scenario, a wide range of band gap combinations get close to maximum STH efficiency value. This is particularly interesting for the material selection—both for the photocathode and for the solar cell—because it relaxes the constraints in the design process of the tandem stack. The maximum value of STH efficiency is now achieved with a 1.88 eV top absorber and a 1.43 eV bottom absorber. Noticeably, high-efficiency PSCs already match this band gap requirement, further simplifying the target accomplishment.

Interestingly, the OPV community already provided means to lower the voltage losses coming from non-radiative recombination in the range of 0.2–0.3 V, comparable with our short-term target (Li et al., 2017; Menke et al., 2018). The same holds true for the external radiative efficiency and IPCE.

Table 2. Parameters employed to simulate the optimized HPC-PSC tandem cell for the short-term optimization scenario (10% STH), using parameters from the sensitivity analysis

	HPC	PSC
Normalized R_s	0.05	0.05
Normalized R_{sh}	10^2	10^2
V_{Loss} [V]	0.3	–
IPCE	0.695	0.8
ERE	10^{-6}	10^{-5}
$J_{cat, c}$ [mA/cm ²]	0.5	–
$J_{cat, a}$ [mA/cm ²]	0.05	–

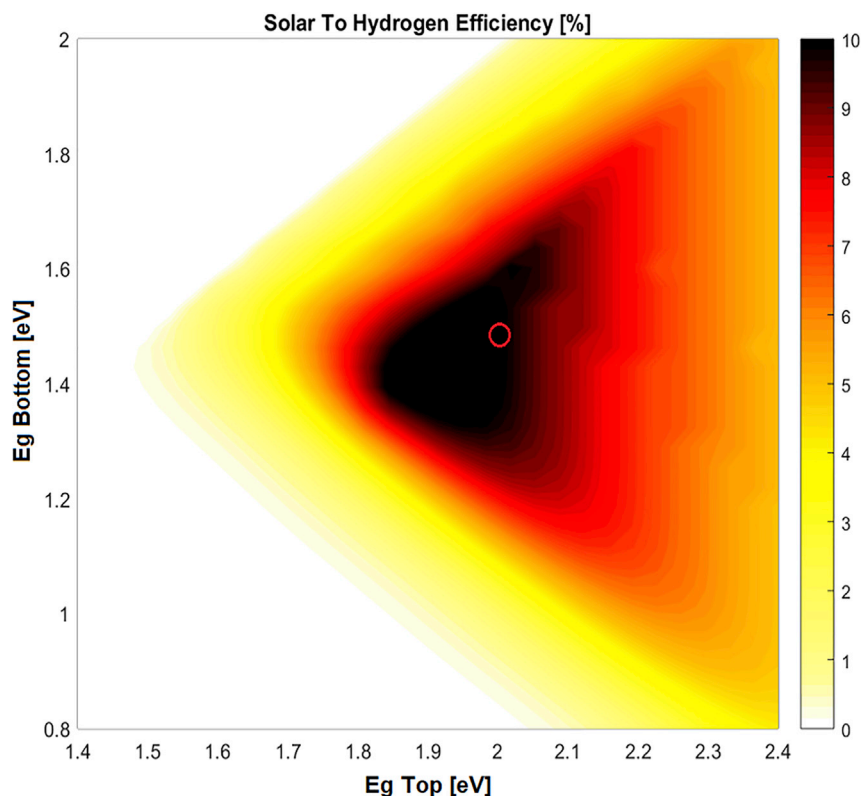


Figure 5. STH efficiency as a function of the band gap of top and bottom absorbers considering the optimized parameters

The red circle identifies the condition of the HPC-PSC employed in this work.

Francàs et al. (2018) moved in this direction, employing the narrow-band-gap, push-pull copolymer PCDTBT (poly[*N*-9'-heptadecanyl-2,7-carbazole-*alt*-5,5-(4',7'-di-2-thienyl-2',1',3'-benzothiadiazole)]) to boost the photovoltage of their HPC in a pH neutral environment. This material closely matches the band gap requirement highlighted in our analysis ($E_G = 1.9$ eV versus a targeted value of 1.88 eV). Therefore, drawing from the library of already available OPV materials that satisfy the given constraints is a straightforward first step. On the other hand, reducing undesired series resistances is a task that needs to be faced taking into consideration both intrinsic material properties and their integration within the whole architecture. Being this parameter often tied to the performances of charge selective layers, their energetic alignment and charge transport properties play a role as important as the photoactive layer in the overall system economy.

Perspective for 20% solar-to-hydrogen

To set a path toward a new efficiency regime for WS devices, we shall look at materials and devices employed in the current state-of-the-art devices on the photovoltaic counterpart. To properly assess the contribution of the PSC element, we simulated the final efficiency of the tandem system when the best performing (23.32% PCE) PSC available in literature (Jiang et al., 2019) is coupled with the HPC and electrocatalyst used in this work. Taking into account the optical shadowing of the opposite photocathode (Figure S11), the estimated STH efficiency of this tandem system is around 2.4% (Figure S12), only slightly better than the value actually obtained in this work. This result corroborates the idea that the main focus should be placed on the optimization of the hybrid photocathode rather than relying only on high-efficiency PV-biasing cells. Instead, a hypothetical HPC with performances similar to the current state-of-the-art OPV cell (Yuan et al., 2019) would have a striking impact on the performances of the overall tandem system. By fitting the JV curve of this benchmark cell (parameters shown in Table 3) and superimposing it to a polarization curve of an hydrogen evolution reaction catalyst, the resulting simulated HPC may be coupled with the employed PSC to obtain a new STH landscape, as shown in Figure 6. In this framework, STH efficiency as high as 19% is expected for a combination of 1.6 eV/1.1 eV photoactive elements.

Table 3. Parameters employed to simulate the HPC-PC tandem cell for the long-term optimization scenario (20% STH), using state-of-the-art OPV solar cell parameters to model the performance of the HPC

	HPC	PSC
Normalized R_s	0.045	0.05
Normalized R_{sh}	10^2	10^2
V_{Loss} [V]	0.1	-
IPCE	0.83	0.8
ERE	10^{-4}	10^{-5}
$J_{cat,c}$ [mA/cm ²]	1	-
$J_{cat,a}$ [mA/cm ²]	0.05	-

These values are, in principle, both within reach given that the current lower limit for perovskite band gaps is around 1.15 eV with Sn instead of Pb as cation (Noel et al., 2014; Rajagopal et al., 2017; Shao et al., 2018; Zhao et al., 2017) and the wide variety of accessible chemistries and properties of organic semiconductors achievable by synthetic chemistry (Baran et al., 2017; Cheng et al., 2018a; Li et al., 2017). It should be mentioned that, as of today, several issues connected to the processing, charge mobility, and recombination of Sn-based PSC need to be faced to achieve substantial PCE. Nevertheless, it is reasonable to forecast that the growing interest in low-band gap perovskites (Zhao et al., 2017) for tandem PSC will accelerate in the close future the development of PSC based on them.

Indeed, the STH we just estimated is based on the outstanding improvements of the field of OPV and PSC and bodes well for the future improvements that the field of HOPEC is capable of. Furthermore, this value almost doubles the minimum threshold in terms of efficiency, which these systems are called to fulfill. While inferring that the field of HOPEC may reach the same efficiency as OPV in the short term may be an optimistic view, we can look up to this result highlighting how dedicated material research and device optimization played a major role. For HOPEC-WS this calls in the first place to identify, or specifically design, organic semiconductors that can withstand the harsh environment of the electrochemical cell. Additionally, novel high-performing BHJ characterized by an extended light harvesting region with minimal charge recombination losses represents the best way forward to this high-efficiency regime.

On the other hand, given the harsh environment of the electrochemical cell, the task of designing an efficient architecture, which minimizes R_s , capable of withstanding the working conditions is more challenging from the material point of view. In this regard, material selection and optimization are expected to play a relevant role in enabling the transition to this new regime, as the results achieved in several works on HPC have already been pointed out (Fumagalli et al., 2016).

DISCUSSION

We demonstrate that hybrid organic systems for solar fuel production hold a high potential, despite the recent appearance of organic semiconductors in the field. Starting from the state-of-the-art architecture employing a P3HT:PCBM bulk heterojunction, coupled to a hybrid organic PSC, we achieve an unbiased STH efficiency above 2%. Moving from this promising result, we envisioned a perspective route of development based on the recent breakthrough of the field of OPV, which reached PCE beyond 15%, while demonstrating that record PSC is not strictly needed. Indeed, as our simulated forecast highlights, if an HPC as performing as the record OPV cell shall be realized, an STH approaching 20% may be achieved with an HPC-PSC tandem system. This long-term scenario represents an intriguing, yet very challenging, opportunity, whereas the 10% STH target, a major milestone of WS community, is found to be within reach. In this regard, a sensitivity analysis on the optoelectronic figures of the HPC highlighted the key role of voltage losses, internal quantum efficiency, and series resistance in achieving this goal. Nevertheless, the extension of results from the PV field to the PEC field is not to be considered trivial because many materials used in the first cannot be used in the harsh environment of the second, especially with regard to the key carrier selective layers (i.e., MoO₃, NiO). Moreover, careful selection and screening of existing organic semiconductors that match the target band gap of 1.88 eV is highly desired and encouraged, eventually relying on specifically designed materials. In sum, we describe an encouraging optimization-driven challenge, setting organic-based systems as a promising solution for sustainable solar fuel production.

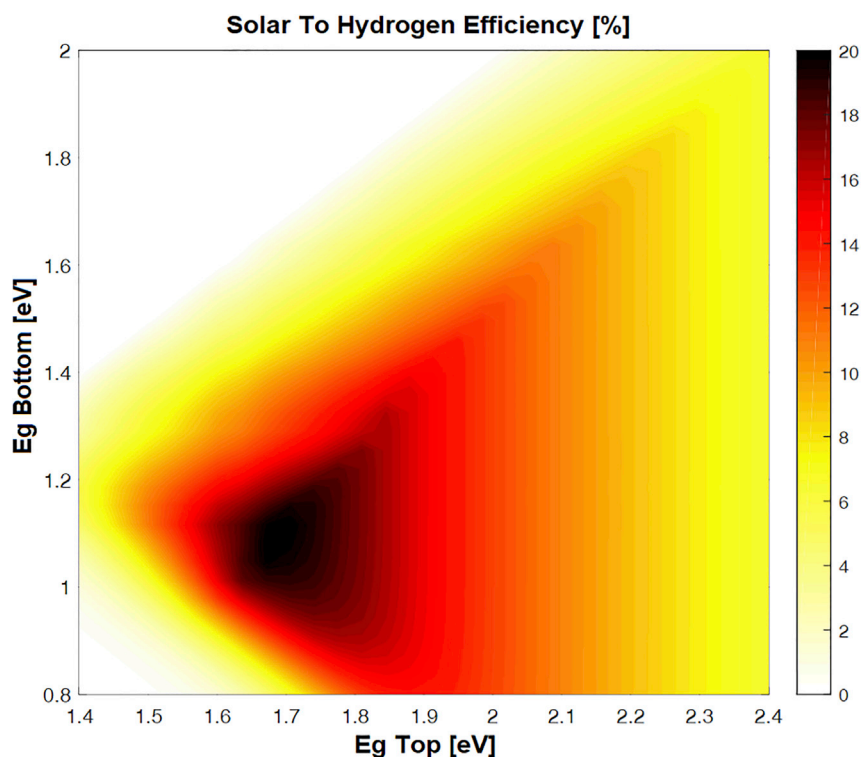


Figure 6. STH contour plot for the 20% STH perspective of organic semiconductors/perovskite solar cell-based tandem system

Limitations of the study

This work focuses on water-splitting tandem systems that employ organic photoactive materials in their PEC- and PV-comprising components, specifically hybrid organic photocathodes and PSCs. The tandem cell presented here stands as the best-performing device in the promising yet limited niche of organic-based PEC-PV (also called HPC-PSC in this work) tandem systems for water splitting. These experimental results and the subsequent theoretical simulations aim to demonstrate that organic-based solutions have the potential to reach the high level of performances already achieved by certain inorganic solutions. The authors hope this work will spark some interest in the scientific community and will encourage others to pursue the potential of organic and hybrid architecture, gradually closing the gap with the scenarios depicted in this work.

Resource availability

Lead contact

Further information and requests for resources should be directed to and will be fulfilled by the lead contact, Fabio Di Fonzo (Fabio.difonzo@iit.it).

Materials availability

This study did not generate new unique materials.

Data and code availability

The data and code supporting the current study are available from the lead contact on request.

METHODS

All methods can be found in the accompanying [transparent methods supplemental file](#).

SUPPLEMENTAL INFORMATION

Supplemental information can be found online at <https://doi.org/10.1016/j.isci.2021.102463>.

AUTHOR CONTRIBUTIONS

A.A., A.M., and F.F. fabricated the photocathode and designed and performed the electrochemical experiments; C.T. fabricated the perovskite solar cell; A.A. and E.R. performed the simulations of the tandem system; F.D.F. and A.P. supervised and coordinated the study. All the authors equally contributed to the interpretation and analysis of data and participated in the manuscript preparation.

DECLARATION OF INTERESTS

The authors declare no competing interests.

Received: November 17, 2020

Revised: March 11, 2021

Accepted: April 20, 2021

Published: May 21, 2021

REFERENCES

- Ahmed, M., and Dincer, I. (2019). A review on photoelectrochemical hydrogen production systems: challenges and future directions. *Int. J. Hydrogen Energy* 44, 2474–2507. <https://doi.org/10.1016/j.ijhydene.2018.12.037>.
- Andrei, V., Hoyer, R.L.Z., Crespo-Quesada, M., Bajada, M., Ahmad, S., De Volder, M., Friend, R., and Reiser, E. (2018). Scalable triple cation mixed halide perovskite–BiVO₄ tandems for bias-free water splitting. *Adv. Energy Mater.* 8, 1–14. <https://doi.org/10.1002/aenm.201801403>.
- Baran, D., Ashraf, R.S., Hanifi, D.A., Abdelsamie, M., Gasparini, N., Röhr, J.A., Holliday, S., Wadsworth, A., Lockett, S., Neophytou, M., et al. (2017). Reducing the efficiency-stability-cost gap of organic photovoltaics with highly efficient and stable small molecule acceptor ternary solar cells. *Nat. Mater.* 16, 363–369. <https://doi.org/10.1038/nmat4797>.
- Bellani, S., Antognazza, M.R., and Bonaccorso, F. (2019). Carbon-based photocathode materials for solar hydrogen production. *Adv. Mater.* 31, 1801446. <https://doi.org/10.1002/adma.201801446>.
- Bellani, S., Najafi, L., Martín-García, B., Ansaldo, A., Del Rio Castillo, A.E., Prato, M., Moreels, I., and Bonaccorso, F. (2017). Graphene-based hole-selective layers for high-efficiency, solution-processed, large-area, flexible, hydrogen-evolving organic photocathodes. *J. Phys. Chem. C* 121, 21887–21903. <https://doi.org/10.1021/acs.jpcc.7b05904>.
- Bornoz, P., Abdi, F.F., Tilley, S.D., Dam, B., Van De Krol, R., Graetzel, M., and Sivula, K. (2014). A bismuth vanadate-cuprous oxide tandem cell for overall solar water splitting. *J. Phys. Chem. C* 118, 16959–16966. <https://doi.org/10.1021/jp500441h>.
- Bornoz, P., Prévot, M.S., Yu, X., Guijarro, N., and Sivula, K. (2015). Direct light-driven water oxidation by a ladder-type conjugated polymer photoanode. *J. Am. Chem. Soc.* 137, 15338–15341. <https://doi.org/10.1021/jacs.5b05724>.
- Chen, M., Liu, Y., Li, C., Li, A., Chang, X., Liu, W., Sun, Y., Wang, T., and Gong, J. (2018a). Spatial control of cocatalysts and elimination of interfacial defects towards efficient and robust CIGS photocathodes for solar water splitting. *Energy Environ. Sci.* 11, 2025–2034. <https://doi.org/10.1039/c7ee03650g>.
- Chen, Q., Fan, G., Fu, H., Li, Z., and Zou, Z. (2018b). Tandem photoelectrochemical cells for solar water splitting. *Adv. Phys. X* 3. <https://doi.org/10.1080/23746149.2018.1487267>.
- Chen, Y., Feng, X., Liu, Y., Guan, X., Burda, C., and Guo, L. (2020). Metal oxide-based tandem cells for self-biased photoelectrochemical water splitting. *ACS Energy Lett.* 5, 844–866. <https://doi.org/10.1021/acscenergylett.9b02620>.
- Cheng, P., Li, G., Zhan, X., and Yang, Y. (2018a). Next-generation organic photovoltaics based on non-fullerene acceptors. *Nat. Photon.* 12, 131–142. <https://doi.org/10.1038/s41566-018-0104-9>.
- Cheng, W.H., Richter, M.H., May, M.M., Ohlmann, J., Lackner, D., Dimroth, F., Hannappel, T., Atwater, H.A., and Lewerenz, H.J. (2018b). Monolithic photoelectrochemical device for direct water splitting with 19% efficiency. *ACS Energy Lett.* 3, 1795–1800. <https://doi.org/10.1021/acscenergylett.8b00920>.
- Cherevko, S., Geiger, S., Kasian, O., Kulyk, N., Grote, J.P., Savan, A., Shrestha, B.R., Merzlikin, S., Breitbach, B., Ludwig, A., and Mayrhofer, K.J.J. (2016). Oxygen and hydrogen evolution reactions on Ru, RuO₂, Ir, and IrO₂ thin film electrodes in acidic and alkaline electrolytes: a comparative study on activity and stability. *Catal. Today* 262, 170–180. <https://doi.org/10.1016/j.cattod.2015.08.014>.
- Clarke, R.E., Giddey, S., Ciacchi, F.T., Badwal, S.P.S., Paul, B., and Andrews, J. (2009). Direct coupling of an electrolyser to a solar PV system for generating hydrogen. *Int. J. Hydrogen Energy* 34, 2531–2542. <https://doi.org/10.1016/j.ijhydene.2009.01.053>.
- Coridan, R.H., Nielander, A.C., Francis, S.a., McDowell, M.T., Dix, V., Chatman, S.M., and Lewis, N.S. (2015). Methods for comparing the performance of energy-conversion systems for use in solar fuels and solar electricity generation. *Energy Environ. Sci.* 8, 2886–2901. <https://doi.org/10.1039/C5EE00777A>.
- Dias, P., Schreier, M., Tilley, S.D., Luo, J., Azevedo, J., Andrade, L., Bi, D., Hagfeldt, A., Mendes, A., Grätzel, M., and Mayer, M.T. (2015). Transparent cuprous oxide photocathode enabling a stacked tandem cell for unbiased water splitting. *Adv. Energy Mater.* 5, 1501537. <https://doi.org/10.1002/aenm.201501537>.
- dos Santos, W.S., Rodriguez, M., Khoury, J.M.O., Nascimento, L.A., Ribeiro, R.J.P., Mesquita, J.P., Silva, A.C., Nogueira, F.G.E., and Pereira, M.C. (2018). Bismuth vanadate photoelectrodes with high photovoltage as photoanode and photocathode in photoelectrochemical cells for water splitting. *ChemSusChem* 11, 589–597. <https://doi.org/10.1002/cssc.201701929>.
- Fountaine, K.T., Lewerenz, H.J., and Atwater, H.A. (2016). Efficiency limits for photoelectrochemical water-splitting. *Nat. Commun.* 7, 1–9. <https://doi.org/10.1038/ncomms13706>.
- Francàs, L., Burns, E., Steier, L., Cha, H., Solà-Hernández, L., Li, X., Shakya Tuladhar, P., Bofill, R., García-Antón, J., Sala, X., and Durrant, J.R. (2018). Rational design of a neutral pH functional and stable organic photocathode. *Chem. Commun.* 54, 5732–5735. <https://doi.org/10.1039/c8cc01736k>.
- Fumagalli, F., Bellani, S., Schreier, M., Leonardi, S., Rojas, H., Ghadirzadeh, A., Tullii, G., Savoini, A., Marra, G., Meda, L., et al. (2016). Hybrid organic-inorganic H₂-evolving photocathodes: understanding the route towards high performances organic photoelectrochemical water splitting. *J. Mater. Chem. A* 4, 2178–2187. <https://doi.org/10.1039/c5ta09330a>.
- Ghadirzadeh, A., Fumagalli, F., Mezzetti, A., Bellani, S., Meda, L., Antognazza, M.R., and Di Fonzo, F. (2018). A three-dimensional architecture for hydrogen-evolving, host/guest, hybrid organic/inorganic photocathodes based on nanolamellar MoO₃ scaffolds. *ChemPhotoChem* 2, 283–292. <https://doi.org/10.1002/cptc.201700159>.
- Gu, P., Wang, Z., Xiao, F., Lin, Z., Song, R., Xu, Q., Lu, J., Liu, B., and Zhang, Q. (2017). An ambipolar azaacene as a stable photocathode for metal-free light-driven water reduction. *Mater. Chem. Front.* 495–498. <https://doi.org/10.1039/c6qm00113k>.
- Gurudayal, John. R.A., Boix, P.P., Yi, C., Shi, C., Scott, M.C., Veldhuis, S.A., Minor, A.M., Zakeeruddin, S.M., Wong, L.H., Grätzel, M., and Mathews, N. (2017). Atomically altered hematite for highly efficient perovskite tandem water-

- splitting devices. *ChemSusChem* 10, 2449–2456. <https://doi.org/10.1002/cssc.201700159>.
- Gurudayal, Sabba, D., Kumar, M.H., Wong, L.H., Barber, J., Grätzel, M., and Mathews, N. (2015). Perovskite-hematite tandem cells for efficient overall solar driven water splitting. *Nano Lett.* 15, 3833–3839. <https://doi.org/10.1021/acs.nanolett.5b00616>.
- Haussener, S., Xiang, C., Spurgeon, J.M., Ardo, S., Lewis, N.S., and Weber, A.Z. (2012). Modeling, simulation, and design criteria for photoelectrochemical water-splitting systems. *Energy Environ. Sci.* 5, 9922–9935. <https://doi.org/10.1039/c2ee23187e>.
- Heumüller, T., Mateker, W.R., Sachs-Quintana, I.T., Vandewal, K., Bartelt, J.A., Burke, T.M., Ameri, T., Brabec, C.J., and McGehee, M.D. (2014). Reducing burn-in voltage loss in polymer solar cells by increasing the polymer crystallinity. *Energy Environ. Sci.* 7, 2974–2980. <https://doi.org/10.1039/c4ee01842g>.
- Holmes-Gentle, I., and Hellgardt, K. (2018). A versatile open-source analysis of the limiting efficiency of photo electrochemical water-splitting. *Sci. Rep.* 8, 1–9. <https://doi.org/10.1038/s41598-018-30959-9>.
- Hu, S., Xiang, C., Haussener, S., Berger, A.D., and Lewis, N.S. (2013). An analysis of the optimal band gaps of light absorbers in integrated tandem photoelectrochemical water-splitting systems. *Energy Environ. Sci.* 6, 2984–2993. <https://doi.org/10.1039/c3ee40453f>.
- Jia, J., Seitz, L.C., Benck, J.D., Huo, Y., Chen, Y., Ng, J.W.D., Bilir, T., Harris, J.S., and Jaramillo, T.F. (2016). Solar water splitting by photovoltaic-electrolysis with a solar-to-hydrogen efficiency over 30%. *Nat. Commun.* 7, 1–6. <https://doi.org/10.1038/ncomms13237>.
- Jiang, Q., Zhao, Y., Zhang, X., Yang, X., Chen, Y., Chu, Z., Ye, Q., Li, X., Yin, Z., and You, J. (2019). Surface passivation of perovskite film for efficient solar cells. *Nat. Photon.* 13, 460–466. <https://doi.org/10.1038/s41566-019-0398-2>.
- Karuturi, S.K., Shen, H., Duong, T., Narangari, P.R., Yew, R., Wong-Leung, J., Catchpole, K., Tan, H.H., and Jagadish, C. (2018). Perovskite photovoltaic integrated CdS/TiO₂ photoanode for unbiased photoelectrochemical hydrogen generation. *ACS Appl. Mater. Inter.* 10, 23766–23773. <https://doi.org/10.1021/acsami.8b04855>.
- Kawano, K., and Adachi, C.H. (2009). Evaluating carrier accumulation in degraded bulk heterojunction organic solar cells by a Thermally stimulated current technique. *Adv. Funct. Mater.* 19, 3934–3940. <https://doi.org/10.1002/adfm.200901573>.
- Kim, J.H.J.H.J.H., Jo, Y., Kim, J.H.J.H.J.H., Jang, J.W., Kang, H.J., Lee, Y.H., Kim, D.S., Jun, Y., and Lee, J.S. (2015). Wireless solar water splitting device with robust cobalt-catalyzed, dual-doped BiVO₄ photoanode and perovskite solar cell in tandem: a dual absorber artificial leaf. *ACS Nano* 9, 11820–11829. <https://doi.org/10.1021/acsnano.5b03859>.
- Kirner, J.T., Stracke, J.J., Gregg, B.A., and Finke, R.G. (2014). Visible-light-assisted photoelectrochemical water oxidation by thin films of a phosphonate-functionalized perylene diimide plus CoOx cocatalyst. *ACS Appl. Mater. Inter.* 6, 13367–13377. <https://doi.org/10.1021/am405598w>.
- Li, S., Liu, W., Li, C.Z., Shi, M., and Chen, H. (2017). Efficient organic solar cells with non-fullerene acceptors. *Small* 13, 1–15. <https://doi.org/10.1002/smll.201701120>.
- Li, X., Jia, M., Lu, Y., Li, N., Zheng, Y.-Z., Tao, X., and Huang, M. (2019). Co(OH)₂/BiVO₄ photoanode in tandem with a carbon-based perovskite solar cell for solar-driven overall water splitting. *Electrochim. Acta* 330, 135183. <https://doi.org/10.1016/j.electacta.2019.135183>.
- Luo, J., Steier, L., Son, M.K., Schreier, M., Mayer, M.T., and Grätzel, M. (2016). Cu₂O nanowire photocathodes for efficient and durable solar water splitting. *Nano Lett.* 16, 1848–1857. <https://doi.org/10.1021/acs.nanolett.5b04929>.
- Machui, F., Hösel, M., Li, N., Spyropoulos, G.D., Ameri, T., Søndergaard, R.R., Jørgensen, M., Scheel, A., Gaiser, D., Kreul, K., et al. (2014). Cost analysis of roll-to-roll fabricated ITO free single and tandem organic solar modules based on data from manufacture. *Energy Environ. Sci.* 7, 2792–2802. <https://doi.org/10.1039/c4ee01222d>.
- McCrory, C.C.L., Jung, S., Ferrer, I.M., Chatman, S.M., Peters, J.C., and Jaramillo, T.F. (2015). Benchmarking hydrogen evolving reaction and oxygen evolving reaction electrocatalysts for solar water splitting devices. *J. Am. Chem. Soc.* 137, 4347–4357. <https://doi.org/10.1021/ja510442p>.
- Meng, L., Zhang, Y., Wan, X., Li, C., Zhang, X., Wang, Y., Ke, X., Xiao, Z., Ding, L., Xia, R., et al. (2018). Organic and solution-processed tandem solar cells with 17.3% efficiency. *Science* 361, 1094–1098. <https://doi.org/10.1126/science.aat2612>.
- Menke, S.M., Ran, N.A., Bazan, G.C., and Friend, R.H. (2018). Understanding energy loss in organic solar cells: toward a new efficiency regime. *Joule* 2, 25–35. <https://doi.org/10.1016/j.joule.2017.09.020>.
- Mezzetti, A., Fumagalli, F., Alfano, A., Iadicicco, D., Antognazza, M.R., and Di Fonzo, F. (2017). Stable hybrid organic/inorganic photocathodes for hydrogen evolution with amorphous WO₃ hole selective contacts. *Faraday Discuss.* 198, 433–448. <https://doi.org/10.1039/c6fd00216a>.
- Noel, N.K., Stranks, S.D., Abate, A., Wehrenfennig, C., Guarnera, S., Haghghirad, A.A., Sadhanala, A., Eperon, G.E., Pathak, S.K., Johnston, M.B., et al. (2014). Lead-free organic-inorganic tin halide perovskites for photovoltaic applications. *Energy Environ. Sci.* 7, 3061–3068. <https://doi.org/10.1039/c4ee01076k>.
- Oppedisano, D.K., Jones, L.A., Junk, T., and Bhargava, S.K. (2014). Ruthenium Electrodeposition from aqueous solution at high cathodic overpotential. *J. Electrochem. Soc.* 161, 489–494. <https://doi.org/10.1149/2.0441410jes>.
- Otep, S., Michinobu, T., and Zhang, Q. (2020). Pure organic semiconductor-based photoelectrodes for water splitting. *Sol. RRL*, 1900395. <https://doi.org/10.1002/solr.201900395>.
- Pan, L., Kim, J.H., Mayer, M.T., Son, M.K., Ummadisingu, A., Lee, J.S., Hagfeldt, A., Luo, J., and Grätzel, M. (2018). Boosting the performance of Cu₂O photocathodes for unassisted solar water splitting devices. *Nat. Catal.* 1, 412–420. <https://doi.org/10.1038/s41929-018-0077-6>.
- Pihosh, Y., Turkevych, I., Mawatari, K., Uemura, J., Kazoe, Y., Kosar, S., Makita, K., Sugaya, T., Matsui, T., Fujita, D., et al. (2015). Photocatalytic generation of hydrogen by core-shell WO₃/BiVO₄ nanorods with ultimate water splitting efficiency. *Sci. Rep.* 5, 1–2. <https://doi.org/10.1038/srep11141>.
- Pinaud, B.A., Benck, J.D., Seitz, L.C., Forman, A.J., Chen, Z., Deutsch, T.G., James, B.D., Baum, K.N., Baum, G.N., Ardo, S., et al. (2013). Technical and economic feasibility of centralized facilities for solar hydrogen production via photocatalysis and photoelectrochemistry. *Energy Environ. Sci.* 6, 1983–2002. <https://doi.org/10.1039/C3EE40831K>.
- Qiu, Y., Liu, W., Chen, W., Chen, W., Zhou, G., Hsu, P.-C., Zhang, R., Liang, Z., Fan, S., Zhang, Y., and Cui, Y. (2016). Efficient solar-driven water splitting by nanocone BiVO₄-perovskite tandem cells. *Sci. Adv.* 2, e1501764. <https://doi.org/10.1126/sciadv.1501764>.
- Rajagopal, A., Yang, Z., Jo, S.B., Braly, I.L., Liang, P.W., Hillhouse, H.W., and Jen, A.K.Y. (2017). Highly efficient perovskite-perovskite tandem solar cells reaching 80% of the theoretical limit in photovoltage. *Adv. Mater.* 29, 1–10. <https://doi.org/10.1002/adma.201702140>.
- Rojas, H.C., Bellani, S., Fumagalli, F., Tullii, G., Leonardi, S., Mayer, M.T., Schreier, M., Grätzel, M., Lanzani, G., Di Fonzo, F., and Antognazza, M.R. (2016). Polymer-based photocathodes with a solution-processable cuprous iodide anode layer and a polyethyleneimine protective coating. *Energy Environ. Sci.* 9, 3710–3723. <https://doi.org/10.1039/c6ee01655c>.
- Rojas, H.C., Bellani, S., Sardu, E.A., Fumagalli, F., Mayer, M.T., Schreier, M., Grätzel, M., Di Fonzo, F., and Antognazza, M.R. (2017). All solution-processed, hybrid organic-inorganic photocathode for hydrogen evolution. *ACS Omega* 2, 3424–3431. <https://doi.org/10.1021/acsomega.7b00558>.
- Salvador, M., Wadsworth, A., Egelhaaf, H.-J., Bannock, J.H., Heumüller, T., Gasparini, N., McCulloch, I., de Mello, J.C., Strohm, S., Baran, D., et al. (2017). Burn-in free nonfullerene-based organic solar cells. *Adv. Energy Mater.* 7, 1700770. <https://doi.org/10.1002/aenm.201700770>.
- Sathre, R., Scown, C.D., Morrow, W.R., Stevens, J.C., Sharp, I.D., Ager, J.W., Walczak, K., Houle, F.A., and Greenblatt, J.B. (2014). Life-cycle net energy assessment of large-scale hydrogen production via photoelectrochemical water splitting. *Energy Environ. Sci.* 7, 3264–3278. <https://doi.org/10.1039/C4EE01019A>.
- Shaner, M.R., Atwater, H.A., Lewis, N.S., and McFarland, E.W. (2016). A comparative technoeconomic analysis of renewable hydrogen production using solar energy. *Energy Environ. Sci.* 9, 2354–2371. <https://doi.org/10.1039/c5ee02573g>.

- Shao, S., Liu, J., Portale, G., Fang, H.H., Blake, G.R., ten Brink, G.H., Koster, L.J.A., and Loi, M.A. (2018). Highly reproducible Sn-based hybrid perovskite solar cells with 9% efficiency. *Adv. Energy Mater.* 8, 1702019. <https://doi.org/10.1002/aenm.201702019>.
- Song, Z., McElvany, C.L., Phillips, A.B., Celik, I., Krantz, P.W., Waththage, S.C., Liyanage, G.K., Apul, D., and Heben, M.J. (2017). A techno-economic analysis of perovskite solar module manufacturing with low-cost materials and techniques. *Energy Environ. Sci.* 10, 1297–1305. <https://doi.org/10.1039/c7ee00757d>.
- Steier, L., Bellani, S., Rojas, H.C., Pan, L., Laitinen, M., Sajavaara, T., Di Fonzo, F., Grätzel, M., Antognazza, M.R., and Mayer, M.T. (2017). Stabilizing organic photocathodes by low-temperature atomic layer deposition of TiO₂. *Sustain. Energy Fuels* 1, 1915–1920. <https://doi.org/10.1039/c7se00421d>.
- Steier, L., and Holliday, S. (2018). A bright outlook on organic photoelectrochemical cells for water splitting. *J. Mater. Chem. A* 6, 21809–21826. <https://doi.org/10.1039/C8TA07036A>.
- Tao, C., Van Der Velden, J., Cabau, L., Montcada, N.F., Neutzner, S., Srimath Kandada, A.R., Marras, S., Brambilla, L., Tommasini, M., Xu, W., et al. (2017). Fully solution-processed n-i-p-Like perovskite solar cells with planar junction: how the charge extracting layer determines the open-circuit voltage. *Adv. Mater.* 29, 1–7. <https://doi.org/10.1002/adma.201604493>.
- Temburne, S., Nandjou, F., and Haussener, S. (2019). A thermally synergistic photoelectrochemical hydrogen generator operating under concentrated solar irradiation. *Nat. Energy* 4, 399–407. <https://doi.org/10.1038/s41560-019-0373-7>.
- Urbain, F., Smirnov, V., Becker, J.P., Lambert, A., Yang, F., Ziegler, J., Kaiser, B., Jaegermann, W., Rau, U., and Finger, F. (2016). Multijunction Si photocathodes with tunable photovoltages from 2.0 v to 2.8 v for light induced water splitting. *Energy Environ. Sci.* 9, 145–154. <https://doi.org/10.1039/c5ee02393a>.
- Wang, L., Yan, D., Shaffer, D.W., Ye, X., Layne, B.H., Concepcion, J.J., Liu, M., and Nam, C.Y. (2018). Improved stability and performance of visible photoelectrochemical water splitting on solution-processed organic semiconductor thin films by ultrathin metal oxide passivation. *Chem. Mater.* 30, 324–335. <https://doi.org/10.1021/acs.chemmater.7b02889>.
- Wu, L., Zang, H., Hsiao, Y.C., Zhang, X., and Hu, B. (2014). Origin of the fill factor loss in bulk-heterojunction organic solar cells. *Appl. Phys. Lett.* 104, 153903. <https://doi.org/10.1063/1.4871582>.
- Xu, P., Feng, J., Fang, T., Zhao, X., Li, Z., and Zou, Z. (2016). Photoelectrochemical cell for unassisted overall solar water splitting using a BiVO₄ photoanode and Si nanoarray photocathode. *RSC Adv.* 6, 9905–9910. <https://doi.org/10.1039/c5ra20115b>.
- Yang, W., Park, J., Kwon, H.C., Hutter, O.S., Phillips, L.J., Tan, J., Lee, H., Lee, J., Tilley, S.D., Major, J.D., and Moon, J. (2020). Solar water splitting exceeding 10% efficiency: via low-cost Sb₂Se₃ photocathodes coupled with semitransparent perovskite photovoltaics. *Energy Environ. Sci.* 13, 4362–4370. <https://doi.org/10.1039/d0ee02959a>.
- Yao, L., Guijarro, N., Boudoire, F., Liu, Y., Rahmanudin, A., Wells, R.A., Sekar, A., Cho, H.H., Yum, J.H., Le Formal, F., and Sivula, K. (2020). Establishing stability in organic semiconductor photocathodes for solar hydrogen production. *J. Am. Chem. Soc.* 142, 7795–7802. <https://doi.org/10.1021/jacs.0c00126>.
- Yao, L., Rahmanudin, A., Guijarro, N., and Sivula, K. (2018). Organic semiconductor based devices for solar water splitting. *Adv. Energy Mater.* 8, 1802585. <https://doi.org/10.1002/aenm.201802585>.
- Young, J.L., Steiner, M.A., Döschner, H., France, R.M., Turner, J.A., and Deutsch, T.G. (2017). Direct solar-to-hydrogen conversion via inverted metamorphic multi-junction semiconductor architectures. *Nat. Energy* 2, 1–8. <https://doi.org/10.1038/nenergy.2017.28>.
- Yuan, J., Zhang, Y., Zhou, L., Zhang, G., Yip, H.L., Lau, T.K., Lu, X., Zhu, C., Peng, H., Johnson, P.A., et al. (2019). Single-junction organic solar cell with over 15% efficiency using fused-ring acceptor with electron-deficient core. *Joule* 3, 1140–1151. <https://doi.org/10.1016/j.joule.2019.01.004>.
- Zhao, D., Yu, Y., Wang, C., Liao, W., Shrestha, N., Grice, C.R., Cimaroli, A.J., Guan, L., Ellingson, R.J., Zhu, K., et al. (2017). Low-bandgap mixed tin-lead iodide perovskite absorbers with long carrier lifetimes for all-perovskite tandem solar cells. *Nat. Energy* 2, 1–7. <https://doi.org/10.1038/nenergy.2017.18>.

iScience, Volume 24

Supplemental information

**Photoelectrochemical water splitting by hybrid
organic-inorganic systems: setting the path
from 2% to 20% solar-to-hydrogen conversion efficiency**

Antonio Alfano, Alessandro Mezzetti, Francesco Fumagalli, Chen Tao, Eugenio Rovera, Annamaria Petrozza, and Fabio Di Fonzo

Supplemental Information

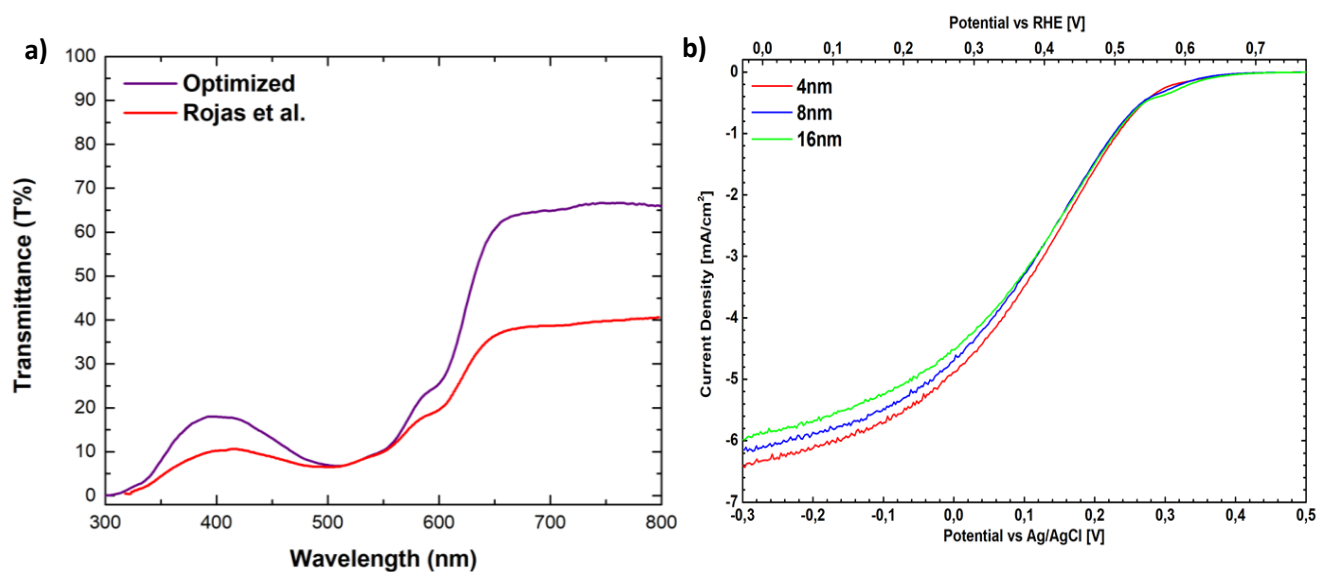


Figure S1. Properties of the HPC for the platinum optimization process. a) Transmission spectra of the optimized photocathode and the original one by Rojas et al. (Rojas et al., 2016); b) Polarization curves of photocathodes with different values of the platinum catalyst layer thickness. Related to Figure 2a (green line).

Deposition Parameter	Rojas et al. (Rojas et al., 2016)	Optimized
Thickness [nm]	100	100
Background Gas	Ar/H ₂ 3.1% mol	Ar/H ₂ 3.1% mol
Background Gas Pressure [Pa]	15	45
Pulse Energy [mJ]	400	300
Repetitio Rate [Hz]	20	20
Fluence [J cm ⁻²]	2.5	2

Table S1. Comparison of deposition parameters for the benchmark HPC and the optimized version used in this work. Related to Figure 2a (green line).

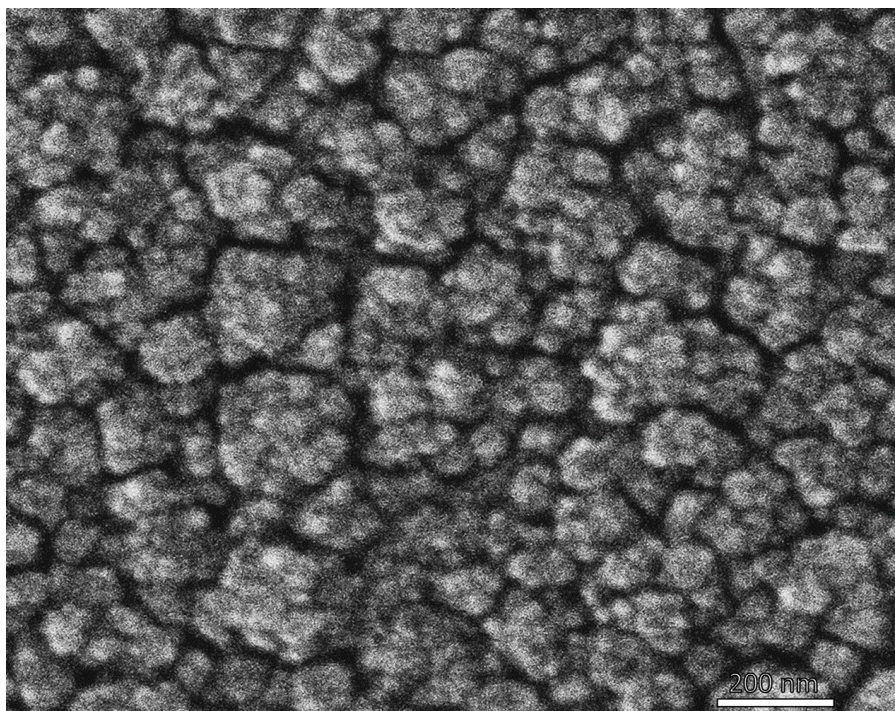


Figure S2. Top-view SEM image of the nanostructured TiO₂ layer as a result of the optimized deposition conditions. Related to Figure 2a (green line).

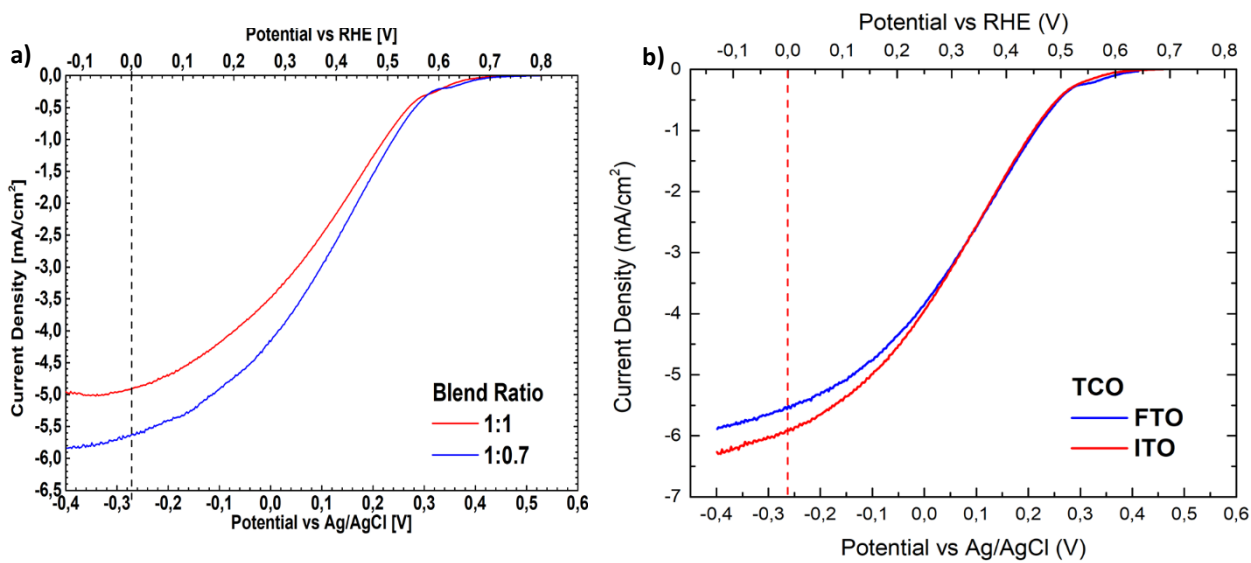


Figure S3. Polarization curve of the photocathode showing the influence of a) D/A ratio of the bulk heterojunction and b) different TCO substrate for the CuI deposition. Related to Figure 2a (green line).

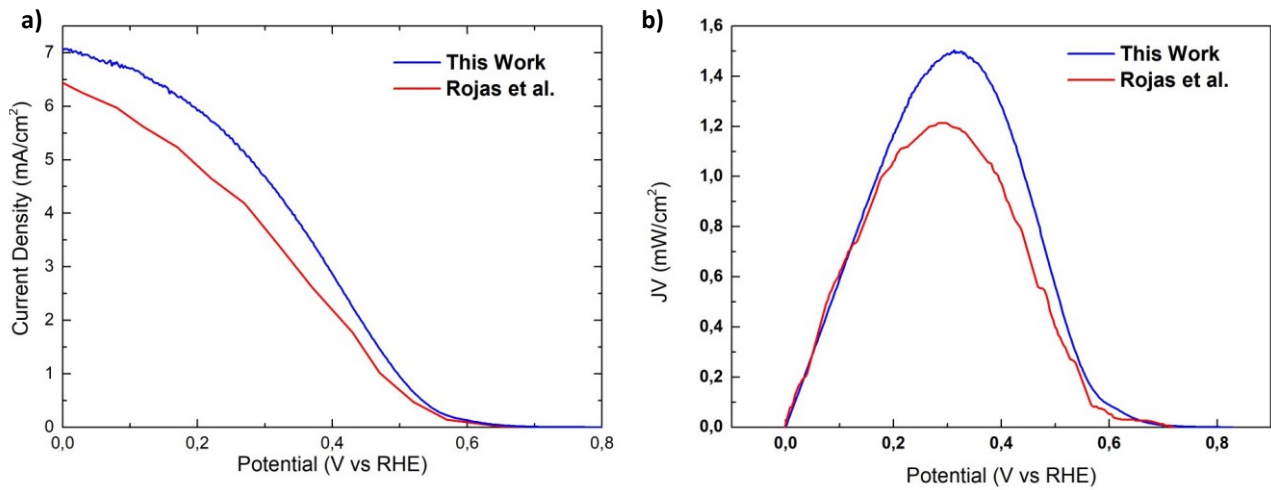


Figure S4. Performance comparison using a) polarization curve and b) ratiometric power saved for the optimized photocathode used in this work and the original version by Rojas et al. (Rojas et al., 2016). Related to Figure 2a (green line).

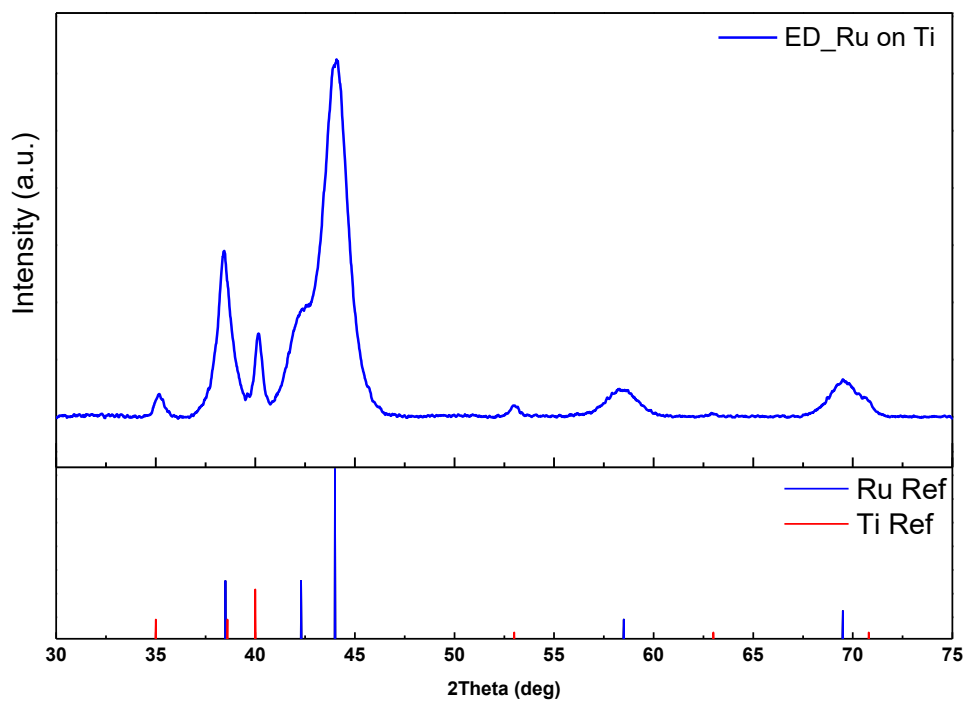


Figure S5. Grazing incidence X-ray diffraction of the electrodeposited Ru catalyst on Ti sheet substrate, compared with the reference peaks for crystalline Ru and Ti. Related to Figure 2a (purple line).

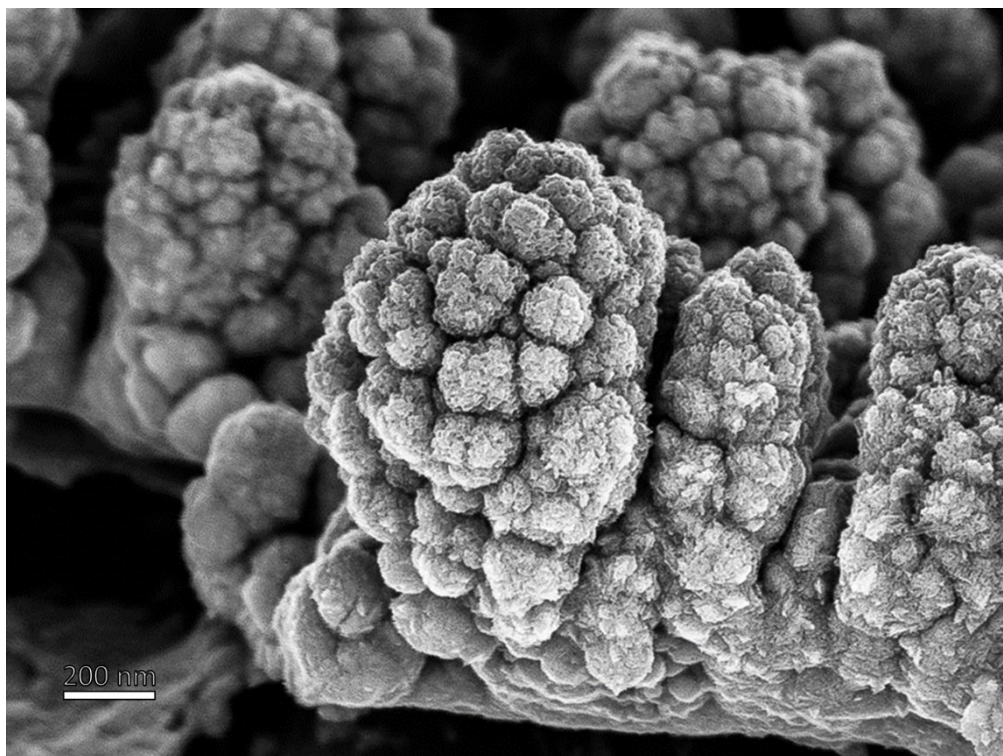


Figure S6. Cross sectional SEM image of the electrodeposited Ru catalysts. Related to Figure 2a (purple line).

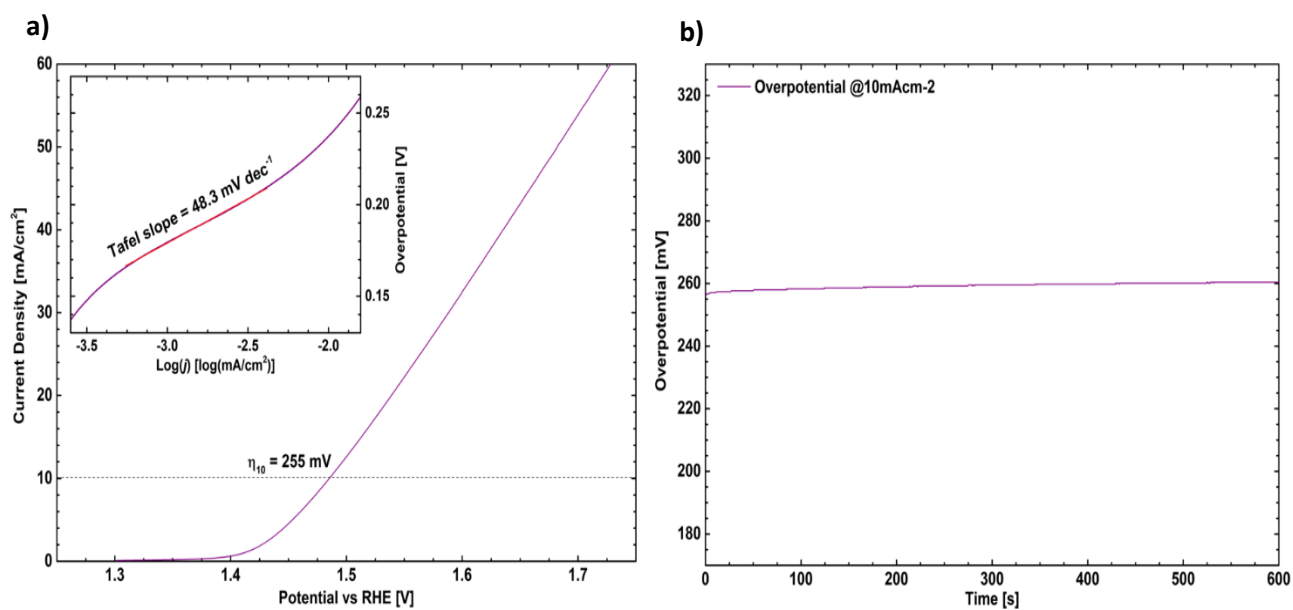


Figure S7. Electrochemical performance of the nanostructured Ru electrocatalyst: a) polarization curve with the η_{10} and the Tafel slope values (inset) and b) chronopotentiometry performed at 10 mA cm^{-2} over the first 10 minutes of operation. Related to Figure 2a (purple line).

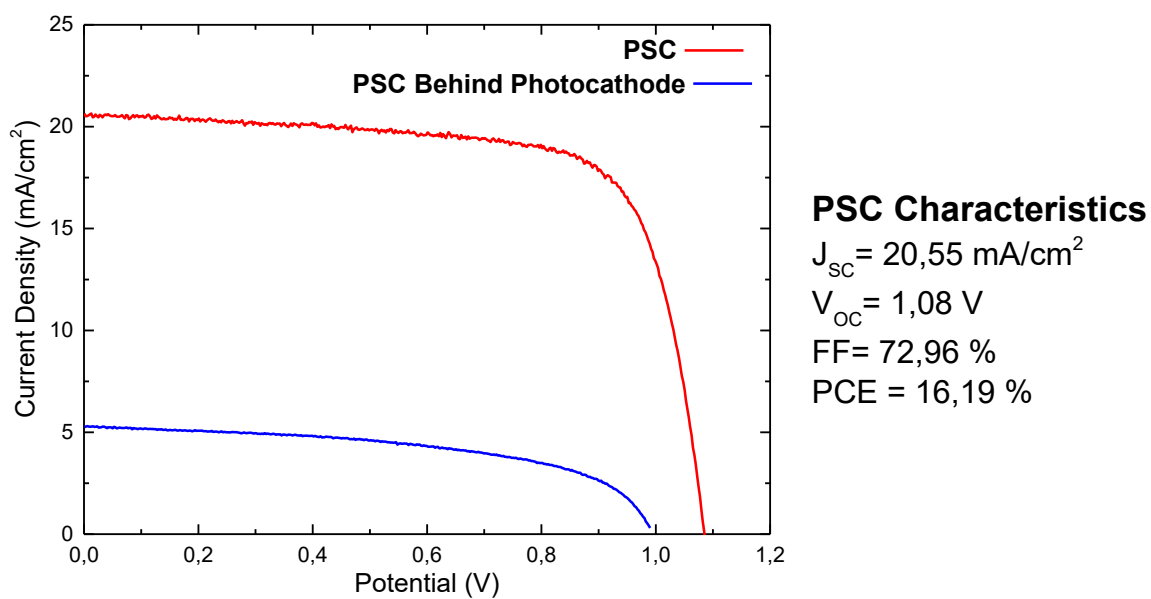


Figure S8. Electrical characterization of the employed PSC under full light (red line) and behind the HPC (blue line). Related to Figure 2a (wine line).

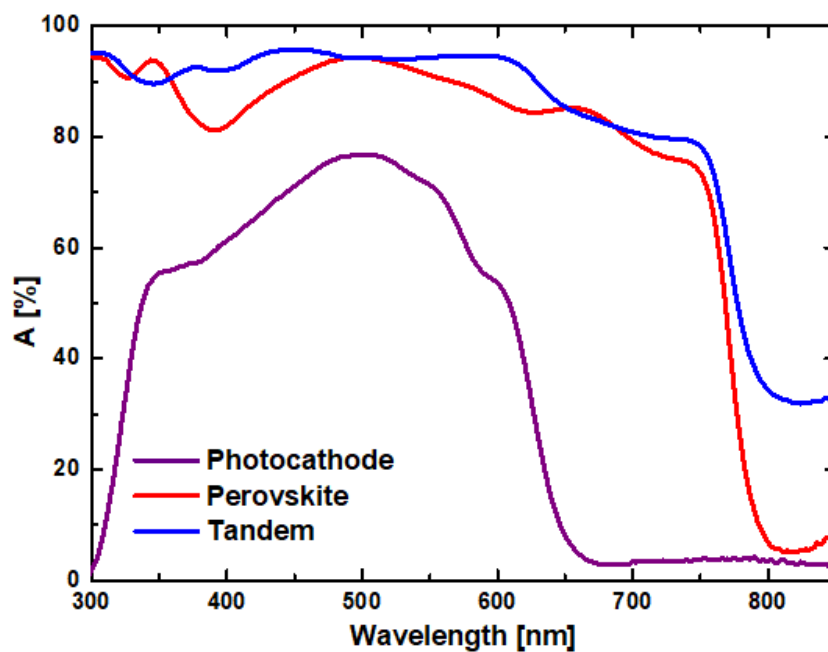


Figure S9. Absorption contribution of the photoactive layers of the photocathode, perovskite solar cell and of the full tandem stack. Related to Figure 3.

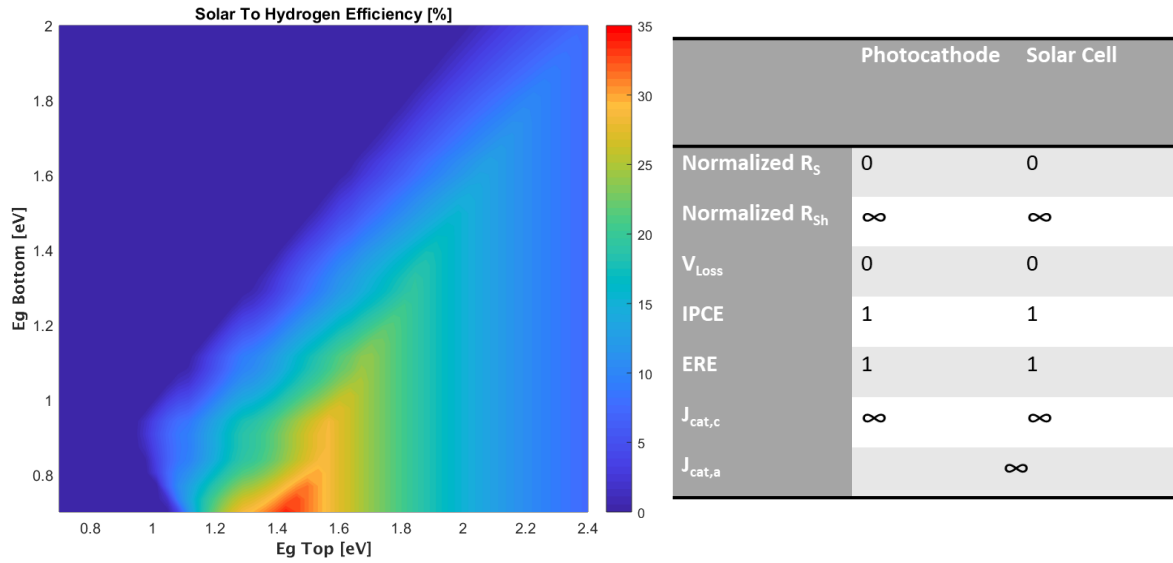


Figure S10. STH contour plot for the ideal case and tabled parameters employed in the simulation. Related to Figure 4.

Parameter	$ \partial\text{STH}/\partial P $
R_s	4,73
R_{sh}	$\approx 10^{-2}$
IPCE	2,49
V_{Loss}	14,71
$J_{cat,c}$	1,5

Table S2. STH partial derivatives (absolute values) with respect to the HPC related parameters. Related to Figure 4.

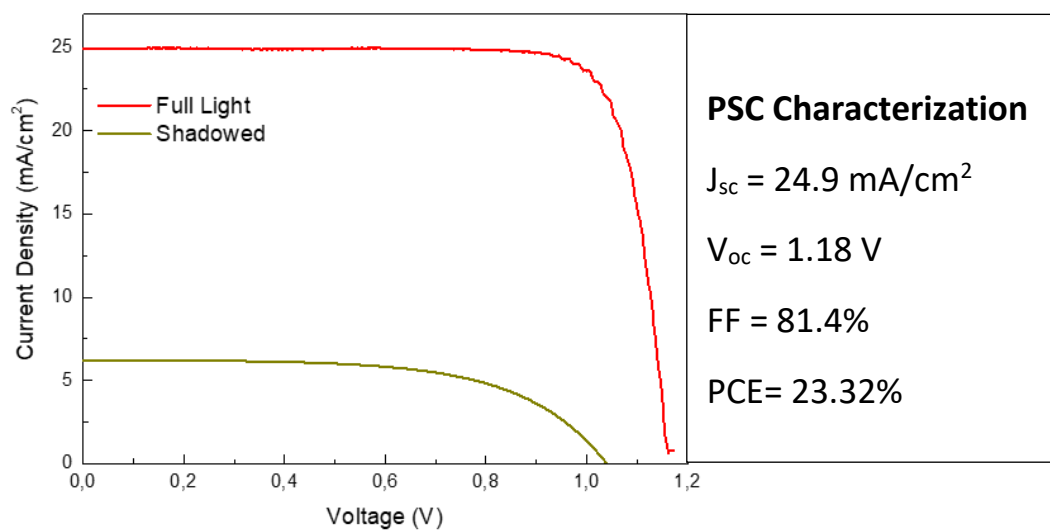


Figure S11. Electrical characteristics of the PSC by Jiang et al. (Jiang et al., 2019) under full illumination (red line) and the estimated behaviour of the cell when shadowed behind the HPC used in this work (green line). Related to Figure 4.

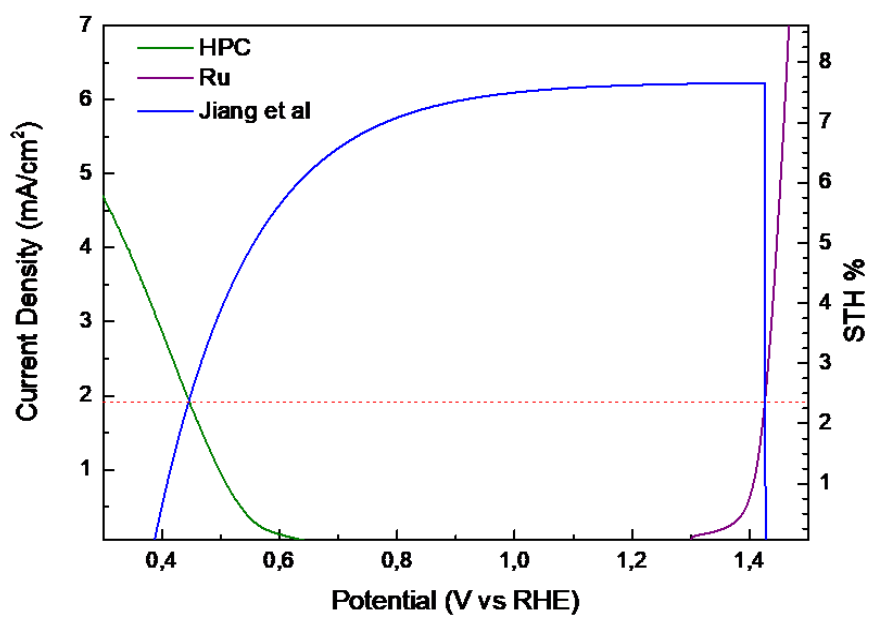


Figure S12. Expected curve matching of the individual components, corresponding expected working point and expected STH efficiency (red dotted line) for the tandem system employing the PSC of Jiang et al. (Jiang et al., 2019). Related to Figure 4.

Transparent Methods

Photocathode Fabrication

Indium-doped tin oxide (ITO) coated glass substrates (20 x 15 mm, sheet resistance 15 Ohm sq^{-1}) are cleaned through a series of sonication baths (20 minutes each) in DI water with Hellmanex™ 3%, isopropanol and acetone. Substrates are then dried overnight in a muffle furnace at 250°C. For the deposition of the HSL, a solution of cuprous iodide (CuI, Sigma Aldrich, 97% purity) 10 mg/mL in Anhydrous Acetonitrile is prepared in N₂ filled glovebox and stirred overnight prior utilization. The cleaned ITO-coated glasses undergo a plasma-treatment in an inductively coupled reactor (100 W RF power, 40 Pa of O₂ gas process pressure) for 15 minutes. Spin coating of the CuI solution is performed in a N₂ filled glovebox at 4000 rpm for 1 minute. For the P3HT:PCBM BHJ, the donor (poly(3-hexylthiophene-2,5-diyl) avg. M_n 15 000–45 000, electronic grade, Sigma Aldrich) and acceptor([6,6]-phenyl-C₆₁-butyric acid methyl ester, 99.5% purity, NanoC) material are separately weighted and dissolved in chlorobenzene. The vials are stirred on a hotplate for 2 hours at 60°C and then mixed to achieve a final blend concentration of 50 mg/mL, with a 1:0.7 D/A ratio. Prior to spin coating, the solution is stirred overnight at 60°C. Photoactive layers of approx. 200nm are achieved by spin coating (Laurell Tech. Corp spin coater) 80 μL of the blend solution on top of the HSL at 1600 rpm rotation speed for 60s. The electron selective layer (ESL) and catalyst layer are deposited in a vacuum chamber by means of pulsed laser deposition (PLD) and magnetron sputtering respectively. The 100-nm-thick nanostructured TiO₂ ESL is deposited starting from a TiO₂ target (Kurt J. Lesker, purity 99.99%) ablated in Ar/H₂ atmosphere (H₂ molar content 3.1%, 45 Pa total pressure) with a pulsed excimer laser (Coherent KrF; $\lambda=248$ nm) with a total energy fluence of 2 J cm^{-2} . The Pt catalytic layer is deposited via magnetron sputtering using a Pt target (Testbourne, purity 99.99%) at an operating pressure of 15 Pa. photocathode fabrication is concluded with a thermal treatment (10 minutes, 130°C) performed in a N₂ glovebox. A Vinyl tape mask is then applied to define an active area of 0.2 cm^2 .

Ruthenium Catalyst Fabrication

The Ruthenium OER catalyst was deposited on a masked Titanium foil (active area 0.066 cm^2) via electrodeposition, following the procedure reported by Oppedisano et al. (Oppedisano et al., 2014) The fabrication recipe selected for this work uses an aqueous solution of 0.25 M HClO₄ and 0.25 mM RuCl₃·xH₂O as the electrolytic precursor and a potentiostatic electrodeposition at -5 V_{RHE} for 300 s, always preceded by the galvanostatic alternating pulse sequence described in the paper, in order to promote an homogeneous nucleation of the film on the substrate. Despite the difference in the substrate used – Oppedisano uses a Silicon wafer coated with titanium (10 nm) and gold (150 nm) – the morphology of the electrodeposited Ruthenium film shown in the SEM images (Figure S5) matches with the one reported in the source paper for the same fabrication recipe. For this reason, the authors consider it plausible to use the reported values of roughness factor (RF) also in this work, at least as an indicative value.

Perovskite Solar Cell Fabrication

Prior to the device fabrication, FTO-coated glass sheets are etched with zinc powder and concentrated HCl to obtain the required electrode pattern. The substrates are then cleaned in an ultrasonic bath of distilled water with detergent, distilled water, acetone and 2-propanol, respectively, for a duration of 5 min for each bath. The substrates are then dried with a clean N₂ flow and finally treated with oxygen plasma to remove the last traces of organic residues. A TiO₂ precursor solution is spin-coated at 2000 rpm for 40 s and then sintered at 500 °C. Once cooled, the samples are transferred into a N₂-filled glove box for the deposition of the cross-linked [6,6]-phenyl-C₆₁-butyric styryl dendron ester (C-PCBSD) layer. For this process, C-PCBSD is dissolved in anhydrous chlorobenzene (10 mg mL⁻¹) and is then spin-coated on top of the TiO₂ layer at 4000 rpm for 30 s, followed by a thermal annealing process on a hotplate at 160 °C for 30 min. For the fabrication of the methylammonium lead iodide (MAPI) perovskite photoabsorbing layer, PbI₂ is dissolved in dimethylformamide (DMF) (700 mg mL⁻¹), the solution is heated and spin-cast at 6000 rpm for 30 s on the FTO/TiO₂/C-PCBSD substrates and immediately dried at 110 °C for 5 min on a hotplate. Then, a methylammonium iodide (MAI) solution (85 mg mL⁻¹) is spin-cast at 3000 rpm for 30 s and the samples are then annealed at 105 °C for 1 h in air. The solution for the hole transporting material is prepared by dissolving 72.3 mg of spiro-MeOTAD, 28.8 μL of 4-tert-butylpyridine and 17.5 μL of a 520 mg mL⁻¹ stock solution of lithium bis(trifluoromethylsulphonyl)imide in acetonitrile into 1 mL of anhydrous chlorobenzene. This hole transporting material solution is then spin-coated on the samples at 4000 rpm for 30 s. Finally, a 75-nm-thick layer of gold is thermally evaporated through a shadow mask to create a metallic contact on a selected area, thus defining the active area of the overall device.

Characterization

PEC measurements were performed with a Autolab PGSTAT302N potentiostat controlled through Nova1.8 (Metrohm) software. Sample were illuminated with a 300 W Xe light source equipped with AM filters (Lot Quantum Design, model LS0306) calibrated to 1 sun. A quartz cell was filled with sufficient amount of electrolyte to perform the PEC measurements. The electrolyte consists of an aqueous solution of H₂SO₄ (Sigma-Aldrich, 98–95% purity), pH=1.25, vigorously purged with N₂ to remove dissolved molecular oxygen. For three-electrodes EC measurement, Ag/AgCl saturated with KCl and a Pt wire were used as reference and counter electrodes respectively. The three elements (the Ru OER catalyst, the HPC and the PSC) have been separately tested prior assembly of the tandem system. For the HPC and Ru OER catalyst, linear sweep voltammetry at a fixed scan rate of 10 mV/s have been performed in a three-electrode configuration as just described above where the element under test served as working electrode. For the HPC, the measurement was performed under simulated sunlight illumination while the anodic electrocatalyst measurements were performed without illumination. The potentiostat and the solar simulator mentioned before were also used to measure the photocurrent of the Perovskite solar cell, connecting its anodic and cathodic contacts to the instrument and scanning the

potential from the open circuit value to the short circuit condition. While characterizing the performance of the HPC-PSC Tandem, same potentiostat and electrolytic solution have been employed. The PSC was placed in close vicinity of the quartz cell and aligned with HPC, immersed in the solution, so that the photoactive areas are in optical series, as depicted in Figure 1 To define the areas, a shadowing mask has been used (Area = 0.066 cm²).

UV-Visible-NIR absorption of the devices were acquired using a Perkin-Elmer Lambda 1050 spectrophotometer. X-Ray Diffraction measurement have been carried out employing a Bruker D8 Advance diffractometer operating in grazing incidence ($\theta = 2^\circ$) mode with Ge-monochromated Cu K α radiation ($\lambda = 1.5406 \text{ \AA}$) with a 2θ range of 30° - 75° and a step size of 0.02° . SEM images have been acquired using a Zeiss SUPRA40 field-emission scanning electron microscope, with an operating voltage of 5kV and a working distance of 2mm.

The software employed to evaluate the STH contour plot and extrapolate the cells parameters for the simulation was Matlab R2018a, according to an adapted version of the model proposed by Fountaine et al.(Fountaine et al., 2016).

Supplementary Bibliography

Fountaine, K.T., Lewerenz, H.J., Atwater, H.A., 2016. Efficiency limits for photoelectrochemical water-splitting. *Nat. Commun.* 7, 1–9. <https://doi.org/10.1038/ncomms13706>

Jiang, Q., Zhao, Y., Zhang, X., Yang, X., Chen, Y., Chu, Z., Ye, Q., Li, X., Yin, Z., You, J., 2019. Surface passivation of perovskite film for efficient solar cells. *Nat. Photonics* 13, 460–466. <https://doi.org/10.1038/s41566-019-0398-2>

Oppedisano, D.K., Jones, L.A., Junk, T., Bhargava, S.K., 2014. Ruthenium Electrodeposition from aqueous solution at high cathodic overpotential. *J. Electrochem. Soc.* 161, 489–494. <https://doi.org/10.1149/2.0441410jes>

Rojas, H.C., Bellani, S., Fumagalli, F., Tullii, G., Leonardi, S., Mayer, M.T., Schreier, M., Grätzel, M., Lanzani, G., Di Fonzo, F., Antognazza, M.R., 2016. Polymer-based photocathodes with a solution-processable cuprous iodide anode layer and a polyethyleneimine protective coating. *Energy Environ. Sci.* 9, 3710–3723. <https://doi.org/10.1039/c6ee01655c>